CHAPTER 1

SPIN TRANSFER TORQUE: A MULTISCALE PICTURE

YUNKUN XIE[1], IVAN RUNGGER [2], KAMARAM MUNIRA [3], MARIA TSONEVA STAMENOVA [2], STEFANO SANVITO [3], AND AVIK W. GHOSH[1]

[1]Charles L Brown School of Electrical and Computer Engineering, University of Virginia, Charlottesville, VA
[2]School of Physics, AMBER and CRANN Institute, Trinity College, Dublin 2, Ireland
[3]Center for Materials for Information Technology, University of Alabama, Tuscaloosa AL

1.1 Introduction

1.1.1 Background

Due to challenges related to physical and electrical scaling, metal-oxide-semiconductor field-effect transistor (MOSFET)-based memory technology is now suffering from increased power leakage and endurance problems. For instance, static random access memory (SRAM) and dynamic random access memory (DRAM) are both volatile, and cannot maintain data when the supplied power is turned off. SRAM has a relatively high cost and the involvement of six transistors makes it unsuitable for high density integration. DRAM can sustain a very high density but suffers from energy dissipation due to the need to refresh its charge. Replacing volatile memory with non-volatile can eliminate standby power consumption and alleviate some of these problems. A universal memory that fills gaps in the contemporary hierarchy presents

By author Copyright © 2014 John Wiley & Sons, Inc.

a powerful driving force behind the development of fast, high density, non-volatile memory technology.

Magnetic systems are promising candidates for next generation memory due to their intrinsic non-volatility and low dissipation during switching [1]. Two good examples of commercial magnetic storage systems are Hard Disk Drives (HDD) and magnetic random access memories (MRAM). In these systems, information is stored in the magnetization direction of nanometer sized magnets, while the switching/writing process is driven by an external magnetic field. In HDD the separation of the read/write head from the storage units allows high density integration of nanomagnets, but the data can only be accessed sequentially. In contrast a MRAM has built-in wires in each memory cell that can generate magnetic fields to switch a magnet at any address. Although these technologies are relatively mature, fundamental scalability issues exist with field switching [2]. The magnetic field is generated by passing a current through a wire, making it hard to scale and creating a large dissipative overhead which dominates the energy cost, even though the switching itself is energy efficient. The extra wires in memory cells also complicate the circuit and raise added concerns on the interference between different cells due to the non-local nature of magnetic field [3].

Spin transfer torque magnetic random access memory (STT-MRAM) offers a novel magnetic memory technology that overcomes some of those difficulties. Instead of field switching, STT-MRAM switches a magnet with a spin-polarized electric current through the so-called spin transfer torque effect (STT). This effect describes the transfer of angular momentum from electrons spin polarized by a fixed magnet and delivered in the form of a torque to flip the magnetization of a free magnetic layer. The use of spin-polarized currents instead of a magnetic field offers a scalable solution for magnetic non-volatile memory. The ultimate goal for STT-MRAM is to replace or at least complement DRAM and/or SRAM to serve as a non-volatile memory in complementary metal oxide semiconductor (CMOS) circuitry. This, of course, requires STT-MRAM to meet all the criteria for conventional memory, such as fast speed, high endurance and low error. Fortunately, STT-MRAM inherits the advantages of MRAM in terms of fast switching (< 10 ns close to SRAM and better than DRAM), very high endurance and non-volatility[4]. The employment of a current switching scheme allows for lower dissipation and high density. The continuous scaling of STT-MRAM has achieved higher density than SRAM and is expected to beat DRAM at the 20 nm technology node in the near future [2].

As promising as STT-MRAM seems, it is not a low power device. In order to switch a magnet with an acceptable endurance, the current density needs to be of the order of $10^{10} - 10^{11}$A/m^2[5, 6], which makes its energy dissipation about two orders of magnitude larger than a CMOS switching energy. To fully capitalize on the ultra-low dissipation intrinsic in magnetization switching, the electric current needs to be eliminated or minimized. A possible route is voltage controlled magnetization, proposed for single-phase or composite multiferroic materials[7]. Multiferroic materials exhibit more than one ferroic order parameter and the coupling between two order parameters, for instance the electrical polarization of a ferro-electric ma-

terial and the magnetization of a ferromagnet, provides control on one another [8]. Over the last decade, a wealth of mechanisms have been proposed as ways to rotate a magnet, ranging from giant spin hall effect (GSHE)[9], thermal torque[10], and strain induced torque[11]. However, robust ultra-low energy magnetic switching still remains an open topic of research.

The application of STT has in the meantime ventured beyond memory. For instance, spin torque oscillators (STO) makes use of STT induced magnetization precession to generated microwave signals from a nanometer scale magnet [12]. STO based networks have been designed to perform complex functions such as pattern recognition [13]. On the other hand, All spin logic (ASL) uses spin for low power computation. The idea in ASL is to avoid spin-charge signal conversion, simplifying the circuit and minimizing energy dissipation [14].

1.1.2 STT modeling: An Integrated approach

In the following sections we will discuss the development of computational tools as well as a broad physical understanding of STT-MRAMs, spanning different materials and device geometries. This will culminate with a multiscale, integrated approach (fig1.1). Given the description of the bandstructure of the magnetic tunnel junction, the transport module is used to calculate the current and the spin torque exerted on the free layer. The calculated spin torque is then fed into the stochastic macrodynamic module which can calculate the changing magnetization of the free layer. The band structure of the tunnel junction can be specified in 3 ways: a fully atomistic model(section 1.3), a parameterized model using continuum grid (section 1.3.2), and a quasi-analytical physics based compact model (section 1.2.1.1). The spin torque exerted on the free magnetic layer can be calculated at two levels of complexity: Non-Equilibrium Green's Function (NEGF) combined with atomistic density functional theory (DFT) or with the parameterized continuum grid bandstructure (section 1.3.2), and a modified Simmons' equation for the quasi-analytical physics based compact model (section 1.2.1.2). Finally, the calculated torque from the transport module is included in the micromagnetic module to calculate the magnetization dynamics in the free layer (section 1.4). The end result is a path from material properties to circuit metrics such as read write errors (e.g. fig 1.24).

What is the merit of such an integrated model? To begin, there already exist material challenges with down scaling, for instance maintaining adequate magnetization with size. Reliable STT-switching has only been observed in a few material systems, despite the large phase space of unexplored magnetic material combinations. A suitable STT material needs to have high spin polarization, high anisotropy, low saturation magnetization and low damping. There are similar constraints on the electronic parameters of the MTJ such as the oxide barrier height and width, and the various longitudinal and transverse electron effective masses in the contacts and the oxide. The merit of an integrated and possibly high throughput combinatorial study is ultimately to provide an overview of the various performance projections and limitations of a wide class of materials before their experimental demonstration.

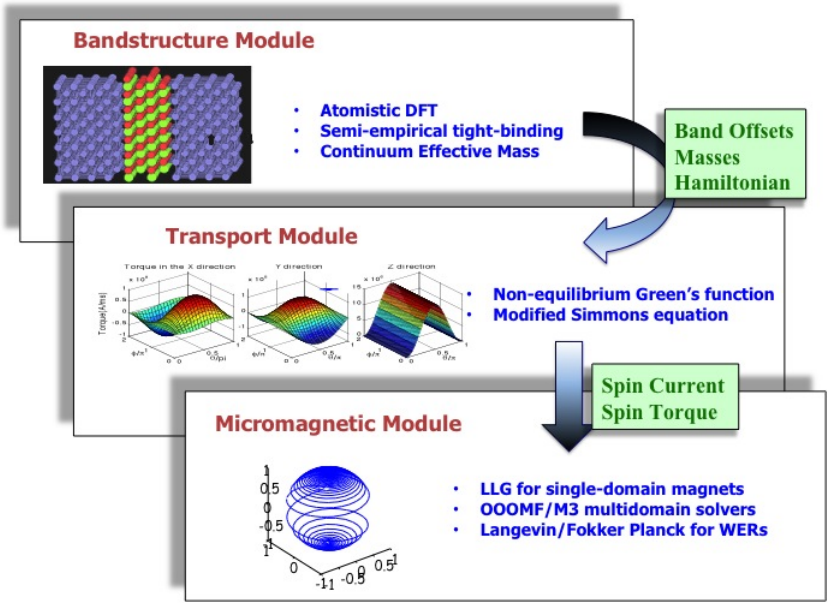

Figure 1.1 Schematic diagram for the integrated approach.

From the point of view of device performance, there are three key metrics that we care about: energy dissipation, switching delay and read/write error. Different criteria apply to each, depending on the particular application. In general, an ideal device should be fast, energy efficient and have a low error rate. However, implementing all three requirements usually requires a subtle trade off among the underlying material and device parameters. For example in STT-MRAM the write error rate can be reduced by increasing the switching current or switching time, but the energy dissipation/speed are compromised as a result. Thus, a simultaneous analysis of the energy delay reliability tradeoff is essential[16].

We start in section 2 with a simple free electron transport model for qualitative understanding of magnetic tunnel junction (MTJ) and spin transfer torque. At this level, it is easy to explain observed features of the switching current, such as the asymmetry between antiparallel to parallel (AP-P), vs parallel to antiparallel (P-AP) switching. We argue that the two processes are intrinsically symmetric, involving either the addition or removal of majority spins on the free magnetic layer. The observed asymmetry comes primarily from the finite spin polarization of the contacts contributing to the current driven torque, and partly from the field like torque due to direct exchange between the layers. In section 3 we present results based on coupling DFT the NEGF method. We use this to explore symmetric filtering in Fe/MgO/Fe to reach a high tunnel magnetoresistance (TMR) and reduce the read current. The method is also used to calculate the corresponding spin torque and write current through 'first principles'. In section 4 the torques are incorporated in the stochastic

Landau-Lifshitz-Gilbert (LLG) equation for the time evolution of the magnetization, or equivalently the Fokker Planck equation for its probability distribution. Analytical and numerical results are presented for the switching delay and write error rate arising from stagnation points in the potential landscape. At the end we show how the separate parts can be combined to give a complete description of STT switching in MTJ, with examples all the way from material to device performance.

1.2 The physics of spin transfer torque

A typical STT-MRAM consists of a magnetic tunnel junction (MTJ) where all important functions arise from the interplay between two ferromagnetic (FM) layers separated by a non-magnetic spacer (Fig 1.2). The FM layers have an intrinsic magnetocrystalline anisotropy that is dependent on the magnetic material used and a demagnetization field which is dependent on the shape of the FM layer. The above two factors result in the FM layer having two bistable states. There can be an additional interface anisotropy between spacer and FM layer[15, 17] that contributes to the overall energy landscape of the free layer. Depending on the orientation its easy axis, the magnetization can be 'in-plane' (easy axis parallel to the junction plane) or 'perpendicular' (easy axis perpendicular to the junction). One of FM layers has fixed magnetization while the other FM is free to rotate its magnetization. Two stable configurations can be established accordingly: FMs with parallel magnetization (P state) or anti-parallel (AP state). One bit information can thereby be encoded into the bi-stable states of MTJ.

The read and write operations are conducted by passing an electric current through the MTJ. For reading, a small voltage is applied across the spacer, causing electrons to tunnel between the FM layers. Inside the FM there exists an internal exchange field that breaks spin degeneracy and shifts the majority-spin, up, electronic states with respect to the minority-spin, down, states (Fig 1.2). Because of the different up and down spin densities of states at the Fermi energy, the electron current through the MTJ becomes different for P and AP configurations, with usually P showing a lower resistance because of the large overlap in states between the magnets, and AP showing a higher resistance because of the reduction in overlap. In other words, the tunneling current $J(\theta)$ and the resistance $R(\theta)$ depend explicitly on the angular orientation θ between the two contact magnetizations. The magneto-resistance ratio TMR $:= (R_{ap} - R_p)/R_p$ has been used to characterize the difference in tunneling resistance between P and AP configuration. With symmetry filtering (discussed in the next section) the TMR ratio in an MTJ can theoretically rise up to more than 2000% [18] in a perfect MTJ junction, with over 200% observed experimentally at room temperature [19]. Such a high TMR is important for differentiating the P/AP configurations, allowing for a lower read current.

The writing operation is performed via the spin transfer torque effect. In 1989, Slonczewski and Berger independently predicted the STT effect in magnetic tunnel junction where two ferromagnets have non-collinear magnetizations [20]. This effect has led to the possibility of current driven control and switching of magnetization in

MTJs. At finite bias, the current gets polarized by the fixed magnet and thus carries angular momentum from one magnet to another. In a spin valve with non-collinear magnetizations, the misalignment between incoming spin and the local magnetic moment induces a torque on both the spins and the magnetization through exchange coupling. In the absence of spin-orbit coupling, this mutual interaction conserves total angular momentum, generating a torque equal to the divergence of the spin current within a given volume (see fig 1.16). This torque ultimately switches the free layer when it exceeds the threshold to overcome the restoring damping forces.

1.2.1 Free-electron model for magnetic tunnel junction

Much of the MTJ switching can be qualitatively understood in terms of a simple free electron model with a spin dependent barrier (Slonczewski, 1989[20]). By matching wave functions across the MTJ boundaries, we get an angle-dependent charge current $J(\theta)$, and thereafter express the TMR ratio in terms of the 'effective polarization' for the MTJ stack. The spin torque, which is perpendicular to the free layer magnetization (the parallel component does not affect the dynamics, can be decomposed into two orthogonal axes as $(\vec{M}_{\text{free}} \times \vec{M}_{\text{fixed}})$ and $\vec{M}_{\text{free}} \times (\vec{M}_{\text{free}} \times \vec{M}_{\text{fixed}})$. These two components will be shown to have completely different symmetries and voltage dependences. In the limit of the magnet being a half-metal (100% spin-polarization), the torques become symmetric and the P-AP/AP-P switching becomes identical.

1.2.1.1 Current and tunnel magnetoresistance

Consider a magnetic tunnel junction. In the free-electron approximation, the longitudinal part of the spin-polarized electron Hamiltonian across the MTJ can be written as:

$$\begin{aligned} H &= \frac{\hbar^2 k_\perp^2}{2m} - \frac{1}{2}\vec{\Delta}\cdot\vec{\sigma}, \quad x<0 \text{ or } x>d \quad \text{(FM contacts)} \\ H &= \frac{\hbar^2 k_\perp^2}{2m^*} + U(x), \qquad 0 \le x \le d \quad \text{(oxide)} \end{aligned} \tag{1.1}$$

where m and m^* are the effective masses in the ferromagnets and the barrier respectively, $\vec{\Delta}$ is the exchange field and $\vec{\sigma} = (\sigma_x, \sigma_y, \sigma_z)$ are the Pauli matrices. If we choose the local z axis to be along the magnetization direction, the energy dispersions of the longitudinal part for two spin channels are two parabolic bands shifted with respect to each other, as shown in fig 1.2. In the following we will simply write $k_{\perp,\uparrow}, k_{\perp,\downarrow}$ as $k_\uparrow, k_\downarrow$.

The magnetic tunnel junction can be broken up into three regions (Fig 1.2): (I) $x < 0$: the left ferromagnetic layer where the magnetization is pinned to the +z axis, (II) $0 \le x \le d$: the insulating tunnel barrier and (III) $x > d$: the right ferromagnetic layer whose magnetization is free to rotate and is defined by the angle θ measured with respect to the positive +z axis. The magnetization of the right ferromagnet is parallel to the z' axis of the coordinate system x',y',z', which is rotated at θ degrees to the original z axis. For simplicity, we first omit the transverse momentum $k_{||}$ and solve for the longitudinal part. The wave function in the three regions can be written

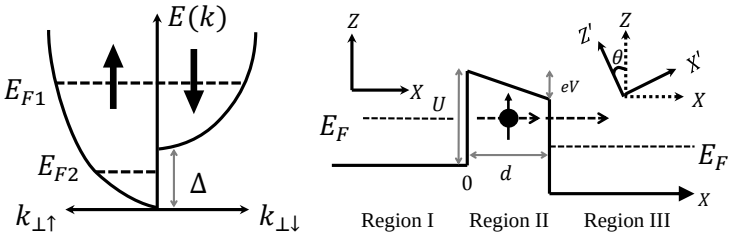

Figure 1.2 Simple barrier model for magnetic tunnel junction. (Left). The band structure of the ferromagnetic contact. The bottom of ↑ and ↓ conduction bands in ferromagnetic(FM) contacts are separated by Δ. E_F is the Fermi energy. If $E_F = E_{F1}$ both spin-up and spin-down channels have non-zero density of states around the Fermi level. If $E_F = E_{F2}$ only spin-up electron exists at the Fermi level and the FM is 100% polarized. (Riight). When a bias is applied on the MTJ, the insulating barrier has a linear ramp potential. d is the width of the insulating barrier and U is is the barrier offset between the contact and the insulator. The magnetization of the right contact is rotated for an angle θ from the magnetization of the left contact.

as:

$$\begin{aligned}
&\text{Region I: } \psi_\uparrow = \tfrac{1}{\sqrt{k^l_\uparrow}} e^{ik^l_\uparrow x} + R_\uparrow e^{-ik^l_\uparrow x} \\
&\qquad\qquad \psi_\downarrow = R_\downarrow e^{-ik^l_\downarrow x} \\
&\text{Region II: } \psi_\sigma = \tfrac{1}{\sqrt{\kappa(E_x,x)}} \left[A_\sigma e^{-E_b(x)} + B_\sigma e^{E_b(x)}\right] \\
&\text{Region III: } \psi'_\sigma = C_\sigma e^{ik^r_\sigma x} \quad \sigma = \uparrow, \downarrow
\end{aligned} \tag{1.2}$$

The longitudinal spin-polarized electron momentum in each of the three region can be expressed as

$$\begin{aligned}
&\text{Region I: } k^l_\uparrow = \frac{1}{\hbar}\sqrt{2mE}, k^l_\downarrow = \frac{1}{\hbar}\sqrt{2m(E-\Delta)} \\
&\text{Region II: } \kappa(E,x) = \frac{1}{\hbar}\sqrt{2m^*[U - eVx/d - E]}, \\
&\qquad\qquad E_b(x) = \int_0^x \kappa(E,x')dx' \\
&\text{Region III: } k^r_\uparrow = \frac{1}{\hbar}\sqrt{2m(E+eV)}, k^r_\downarrow = \frac{1}{\hbar}\sqrt{2m(E-\Delta+eV)}
\end{aligned} \tag{1.3}$$

Notice that the wave function in region III, $\psi'_\uparrow$ and $\psi'_\downarrow$, is written with respect to the local axes, x',y',z'. In order to conform to the original axes, a spinor transformation is required,

$$\begin{aligned}
\psi_\uparrow &= cos(\tfrac{\theta}{2})\psi'_\uparrow + sin(\tfrac{\theta}{2})\psi'_\downarrow \\
\psi_\downarrow &= -sin(\tfrac{\theta}{2})\psi'_\uparrow + cos(\tfrac{\theta}{2})\psi'_\downarrow
\end{aligned} \tag{1.4}$$

By matching $\psi_{\uparrow,\downarrow}$ and $d\psi_{\uparrow,\downarrow}/dx$ at x=0 and d, the unknowns, $R_{\uparrow,\downarrow}$, $A_{\uparrow,\downarrow}$, $B_{\uparrow,\downarrow}$and $C_{\uparrow,\downarrow}$ can be solved for. The charge current is obtained from,

$$J_e = \frac{e\hbar}{2m^* i}\left[\begin{pmatrix}\psi_\uparrow^* & \psi_\downarrow^*\end{pmatrix}\begin{pmatrix}d\psi_\uparrow/dx \\ d\psi_\downarrow/dx\end{pmatrix} - \begin{pmatrix}\psi_\uparrow & \psi_\downarrow\end{pmatrix}\begin{pmatrix}d\psi_\uparrow^*/dx \\ d\psi_\downarrow^*/dx\end{pmatrix}\right] \tag{1.5}$$

Since the charge current is conserved throughout the junction, the equation can be evaluated at any point. Solving for the charge current to the leading order in $e^{-E_b(d)}$[21], we get

$$J_e(E) = J_0(1 + P^2\cos\theta) \tag{1.6}$$

where

$$J_0(E) = \frac{8e\hbar\kappa_L\kappa_R}{m^*}\frac{(\kappa_L^2 + k_\uparrow^l k_\downarrow^l)(k_\uparrow^l + k_\downarrow^l)}{(\kappa_L^2 + k_\uparrow^{l\,2})(\kappa_L^2 + k_\downarrow^{l\,2})}\frac{(\kappa_R^2 + k_\uparrow^r k_\downarrow^r)(k_\uparrow^r + k_\downarrow^r)}{(\kappa_R^2 + k_\uparrow^{r2})(\kappa_R^2 + k_\downarrow^{r2})}e^{-2E_b(d)} \tag{1.7}$$

$$\begin{aligned} P(E)^2 =& \frac{(\kappa_L^2 - k_\uparrow^l k_\downarrow^l)(k_\uparrow^l - k_\downarrow^l)}{(\kappa_L^2 + k_\uparrow^l k_\downarrow^l)(k_\uparrow^l + k_\downarrow^l)} \cdot \frac{(\kappa_R^2 - k_\uparrow^r k_\downarrow^r)(k_\uparrow^r - k_\downarrow^r)}{(\kappa_R^2 + k_\uparrow^r k_\downarrow^r)(k_\uparrow^r + k_\downarrow^r)} \\ =& P_l(\kappa_L, k_\uparrow^l, k_\downarrow^l)P_r(\kappa_R, k_\uparrow^r, k_\downarrow^r) \end{aligned} \tag{1.8}$$

$P_i = (\kappa_i^2 - k_\uparrow^i k_\downarrow^i)(k_\uparrow^i - k_\downarrow^i)(\kappa_i^2 + k_\uparrow^i k_\downarrow^i)^{-1}(k_\uparrow^i + k_\downarrow^i)^{-1}, \quad (i = l, r)$ are defined as 'effective polarization' by Slonczewski because it is the product of the FM contact polarization $(k_\uparrow^i - k_\downarrow^i)(k_\uparrow^i + k_\downarrow^i)^{-1}$ and the coupling between the spacer and the FM contact, $(\kappa_i^2 - k_\uparrow^i k_\downarrow^i)(\kappa_i^2 + k_\uparrow^i k_\downarrow^i)^{-1}$. In order to obtain the total charge current through the MTJ, one needs to sum over the transverse momentum and integrate over energy. The TMR ratio can be related to the effective polarization:

$$\text{TMR} = \frac{I_P - I_{AP}}{I_{AP}} \propto \frac{2P_L P_R}{1 - P_L P_R} \tag{1.9}$$

Note that this is the same formula as the famous Julliere model, except for the interpretation of polarization: Julliere model is rather ambiguous on the definition of spin-polarization (many people interpret it as the spin polarization of the bulk), while Slonczewski model incorporates the coupling between contacts and the barrier.

1.2.1.2 Spin current and torque

The spin current is calculated as

$$J_\sigma(E) = \frac{e\hbar}{2m^* i}\left[\begin{pmatrix}\psi_\uparrow^* & \psi_\downarrow^*\end{pmatrix}\sigma\begin{pmatrix}d\psi_\uparrow/dx \\ d\psi_\downarrow/dx\end{pmatrix} - \begin{pmatrix}\psi_\uparrow & \psi_\downarrow\end{pmatrix}\sigma\begin{pmatrix}d\psi_\uparrow^*/dx \\ d\psi_\downarrow^*/dx\end{pmatrix}\right] \tag{1.10}$$

The spin current is not conserved inside the ferromagnetic contacts because of the presence of the internal exchange field. We therefore evaluate it at $x = 0^+$ within the spacer where it is conserved. As shown in fig 1.16, we calculate the spin current that enters/exits the FM layers and extract the torque, ignoring the z component J_z which has no contribution to the torque.

When the spin current goes from region I to region III, it deposits angular momentum on the right ferromagnet that can switch from the AP to the P configuration. In the meantime, the first region also experiences a torque symmetrically induced by the transverse spin currents due to the removal of angular momentum (however being a fixed layer it stays pinned). This torque is analogous to the one we use for P-to-AP switching, when a negative voltage is applied and angular momentum is removed from the free layer. We will work out below the expressions for the two torques, which we will invoke later on to explain the asymmetry in the switching processes. When electrons are injected from I to III, the torques imposed on regions I and III work out to be

Region I:

$$\begin{aligned}\tau_{x,I}^{I\to III}(E) &= \frac{e\hbar}{2m^*}J_0 P_R \sin\theta \\ \tau_{y,I}^{I\to III}(E) &= -\frac{4e^2\hbar^2}{m^{*2}}\Im\big[\Delta R^l\big]\Re[\Delta R^r]\sin\theta e^{-2E_b(d)}\end{aligned} \tag{1.11}$$

Region III:

$$\begin{aligned}\tau_{x,III}^{I\to III}(E) &= \frac{e\hbar}{2m^*}J_0 P_L \sin\theta \\ \tau_{y,III}^{I\to III}(E) &= \frac{4e^2\hbar^2}{m^{*2}}\Im\big[\Delta R^l\big]\Re[\Delta R^r]\sin\theta e^{-2E_b(d)}\end{aligned} \tag{1.12}$$

where $\Im$ and $\Re$ respectively denote the imaginary and real parts. Here $\Delta R^{l,r} = (R_\uparrow^{l,r} - R_\downarrow^{l,r})/2$ is the difference in reflection coefficient for spin up/down electrons between the non-magnetic barrier and the FM contact. In this free-electron model, the reflection coefficient is $R_{\uparrow,\downarrow}^{l,r} = (i\kappa - k_{\uparrow,\downarrow}^{l,r})/(i\kappa + k_{\uparrow,\downarrow}^{l,r})$.

For electrons injected from region III to region I, the spin transfer torque can be easily written out by making the changes ($l \leftrightarrow r, \theta \leftrightarrow -\theta$) in the above equations. We will see the importance of these four torque expressions later in the chapter.

Region I:

$$\begin{aligned}\tau_{x,I}^{III\to I}(E) &= \tau_{x,III}^{I\to III}(E)(l\leftrightarrow r, \theta\to -\theta) \\ \tau_{y,I}^{III\to I}(E) &= \tau_{y,III}^{I\to III}(E)(l\leftrightarrow r, \theta\to -\theta)\end{aligned} \tag{1.13}$$

Region III:

$$\begin{aligned}\tau_{x,III}^{III\to I}(E) &= \tau_{x,I}^{I\to III}(E)(l\leftrightarrow r, \theta\to -\theta) \\ \tau_{y,III}^{III\to I}(E) &= \tau_{x,I}^{I\to III}(E)(l\leftrightarrow r, \theta\to -\theta)\end{aligned} \tag{1.14}$$

1.2.1.3 Bias-dependent STT Let us only consider the torque in region III (assumed to be free layer). First examine the y component which corresponds to the field like term $\propto \vec{M}_{\text{free}} \times \vec{M}_{\text{fixed}}$ when written in the coordinate independent form.

The total torque can be evaluated by integrating over energy (assume zero temperature for simplicity)

$$\begin{aligned}\tau_y(V) =& \sum_{\vec{k}_{||}} \int_{E_c}^{\infty} (\tau_{y,III}^{I\to III} + \tau_{y,III}^{III\to I}) dE \\ =& \frac{4e^2\hbar^2}{m^{*2}} \sum_{\vec{k}_{||}} \left[\int_{E_c}^{E_{fL}} \sin\theta e^{-2E(d)} \Im[\Delta R^r] \Re[\Delta R^l] dE \right. \\ & \left. + \int_{E_c}^{E_{fR}} \sin\theta e^{-2E(d)} \Im[\Delta R^l] \Re[\Delta R^r] dE \right]\end{aligned} \tag{1.15}$$

with E_c being the bottom of the conduction band. Notice that $\tau_y(V)$ is an even function of V, $\tau_y(V) = \tau_y(-V)$, if the two ferromagnetic contacts are made from the same material. Taylor expanding $\tau_y(V)$ as a function of bias, we get

$$\tau_y(V) \approx \tau_y(0) + \frac{1}{2}\frac{\partial^2 \tau_y}{\partial V^2} V^2 + o(V^4) + \dots \tag{1.16}$$

At low voltage the y component varies quadratically with V and is non-zero even at zero bias, representing the exchange coupling between the two FMs [22]. In other words, the magnets want to orient in parallel/antiparallel (depending on the sign of τ_y, i.e., whether the exchange parameter is ferro or antiferromagnetic), regardless of the sign of the applied bias.

$$\begin{aligned}\tau_y(0) =& \frac{4e^2\hbar^2}{m^{*2}} \sum_{\vec{k}_{||}} \int_{E_c}^{E_f} \sin\theta e^{-2E(d)} \Im[\Delta R^l \Delta R^r] dE \\ \approx& \frac{\hbar^2\kappa^2 e^2}{2\pi^2 m^{*2} d^2} \sin\theta e^{-2\kappa d} \Im[\Delta R^l \Delta R^r]\end{aligned} \tag{1.17}$$

In contrast, when evaluating the x component $\tau_x(V)$ (the current driven Slonczewski torque $\propto \vec{M}_{\text{free}} \times (\vec{M}_{\text{free}} \times \vec{M}_{\text{fixed}})$), we get $\tau_{x,III}^{I\to III} = -\tau_{x,III}^{III\to I}$. The total torque can be evaluated as

$$\begin{aligned}\tau_x(V) =& \sum_{\vec{k}_{||}} \int_{E_c}^{\infty} (\tau_{x,III}^{I\to III} + \tau_{x,III}^{III\to I}) dE \\ =& \sum_{\vec{k}_{||}} \int_{E_f - eV/2}^{E_f + eV/2} \tau_{x,III}^{I\to III}(E) dE \\ \propto& \; J_0(E_f) P_L(E_f) \sin\theta V \quad \text{at low bias}\end{aligned} \tag{1.18}$$

The above equation shows that the current driven torque has a linear variation with V at low bias. In other words, the free magnet gains majority current in one direction and loses it in the opposite bias direction, making the torque antisymmetric. At large bias τ_x deviates from linearity and becomes asymmetric between positive and negative bias, the origin of which we will discuss now.

1.2.1.4 Symmetry in P-to-AP/AP-to-P switching In experiments one observes different switching currents for P-to-AP vs AP-to-P. This difference is often attributed to two different processes involved, with the former arising from majority electrons added to the fixed layer, while the latter arising from minority carriers injected from the free layer and reflected back at the fixed layer/spacer interface to induce P-to-AP switching. This picture is unnecessarily confusing. It would indicate that a fully polarized free layer will have no minority carriers to inject and should not switch P-to-AP (in reality, it switches easier). It would also suggest that increasing the barrier thickness would quickly eliminate the P-to-AP process as the minority carriers must travel through two lengths of the oxide giving twice the tunneling induced decay constant e^{-4E_b}. *In reality, the P-to-AP switching is driven not so much by the addition of reflected minority carrier angular momentum, but instead by the removal of majority carrier angular momentum.* The two processes are operationally 'symmetric' in a sense that in both cases it is the majority carriers (their addition or removal) that determine the free layer switching. In section 1.4 through real-time magnetization dynamics simulation we will show that once the density of minority spin approaches the majority spin density the switching starts to happen, both for AP-to-P and P-to-AP switching. We will then demonstrate that for a half-metallic contact the P-to-AP switching process is not inhibited by the lack of minority carriers, but instead becomes equally efficient.

The observed asymmetry in switching current arises not from the simple difference in majority and minority carrier density of states, but from their energy dependent polarization [21, 24, 25, 26]. To simplify the discussion we assume zero temperature and just look at the electrons injected around the fermi energy (see fig 1.3). The key point is that the torques for the two opposite cases are exerted by spins added to or removed from the fixed layer, involving filled states vs empty states in the two cases that sit at different energies (below vs above the fixed layer Fermi energy). Specifically, when a MTJ switches from AP to P, the polarized electrons are moved from the filled states in the fixed layer lying in the bias window between E_F and $E_F - eV$. From equations 1.11-1.12 we know the torque on the free layer is proportional to the polarization of the fixed layer, which is higher for these low energy states of the fixed layer. For P to AP switching, majority spins are removed from the free layer into the fixed layer empty states sitting between E_F and $E_F + eV$ at a lower polarization. Since the effective torque on the free layer is proportional to the polarization of the fixed layer, we obtain an asymmetric torque ($|\tau_x(V)| \neq |\tau_x(-V)|$).

In the half-metallic limit (see fig 1.2 when $E_F = E_{F2}$) electrons are 100% polarized around the fermi energy with $k_\downarrow^l = ip^l$, $k_\downarrow^r = ip^r$. The previous result for torque τ_x on both Region I and Region III can be simplified and found to be the same (see eq 1.19). The equality is understood by the fact that the polarization is constant so that τ_x is symmetric between positive and negative bias from previous discussion.

$$\tau_{x,I}^{I\to III} = \tau_{x,III}^{I\to III} = \frac{4e^2\hbar^2}{m^{*2}} \frac{\kappa_L \kappa_R k_\uparrow^l k_\uparrow^r}{(\kappa_L^2 + {k_\uparrow^l}^2)(\kappa_R^2 + {k_\uparrow^r}^2)} \sin\theta e^{-2E_b(d)} \tag{1.19}$$

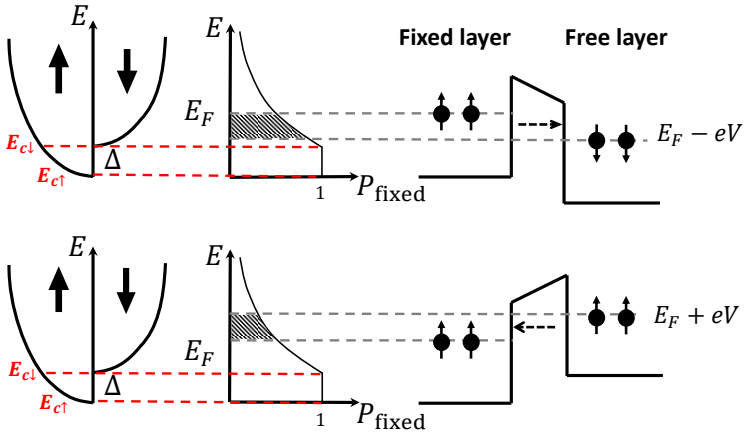

Figure 1.3 Asymmetric torques on the free layer during AP-to-P and P-to-AP switching. Top: AP-to-P switching. Electrons from the fixed layer deposit angular momentum on the free layer. τ_x is related to the polarization of the fixed layer from $E_F - eV$ to E_F. Bottom: P-to-AP switching: Electrons are taken away from the free layer with its angular momentum. The corresponding torque is related to the polarization of the fixed layer from energy E_F to $E_F + eV$. The polarization of the fixed layer is determined by its density of states and is energy depedent when E_F is not in the gap of minority band.

Note that the y component (perpendicular torque) $\tau_y(V) = b(V)\ \vec{M}_{\text{free}} \times \vec{M}_{\text{fixed}}$, where $b(V) \approx B_0 + B_1 V^2$ is the bias dependency, also contributes to the asymmetry in AP-to-P/P-to-AP switching in an in-plane MTJ. A positive value of $b(V)$ prefers the parallel configuration in the MTJ while a negative value prefers the anti-parallel configuration for in-plane free layers, as we see in our micro-magnetic simulations (Fig. 1.4). The switching behavior can be easily understood from the approximate analytical solution to the micro-magnetic model (see section 1.4 for the definition of the parameters), where the critical switching current is modified by the perpendicular torque,

$$I_c - \alpha B_1 = \frac{1}{\eta}\frac{2e}{\hbar}\alpha\mu_0\Omega H_K M_S(1 + \frac{M_S}{2H_K} + \frac{H}{H_K}) \tag{1.20}$$

where H is the effective field due to perpendicular torque at zero voltage, $H = (H_K\hbar\eta B_0)/(4q\Omega K)$, and B_1 is the additional perpendicular torque due to voltage applied. The field like torque at zero voltage increases the thermal stability of the AP configuration and decreases the stability at the P configuration [23].

$$\begin{aligned}\Delta_{AP} &= \frac{H_K M_S \Omega}{2K_B T}\left(1 + \frac{H}{H_K}\right)^2 \\ \Delta_P &= \frac{H_K M_S \Omega}{2K_B T}\left(1 - \frac{H}{H_K}\right)^2\end{aligned} \tag{1.21}$$

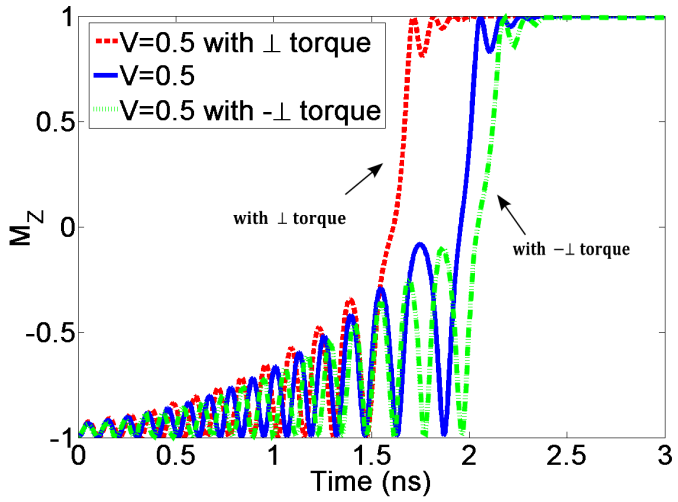

Figure 1.4 Simulation for AP to P switching in an in-plane magnetic layer. Magnetic properties of CoFeB, H_K of 500Oe, M_S of 1050 emu/cc and α of 0.02 are used. Positive perpendicular torque helps AP to P switching while a negative perpendicular torque delays the switching.

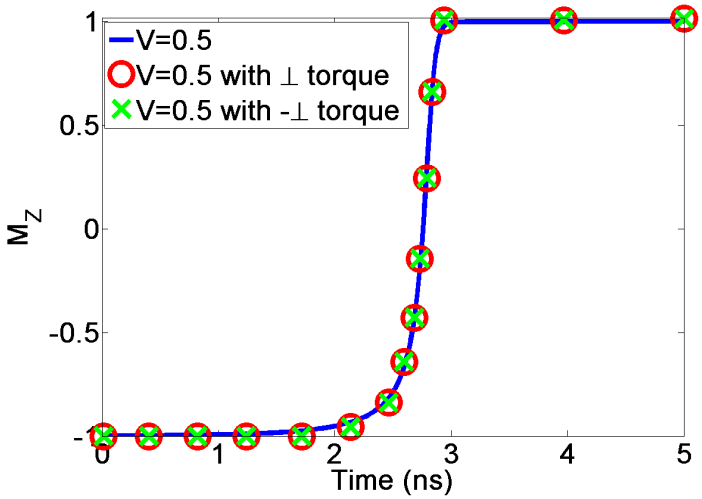

Figure 1.5 Simulation for AP to P switching in a perpendicular magnetic layer. Magnetic properties of CoPd, H_K of 20,000Oe, M_S of 450 emu/cc and α of 0.1 are used. The perpendicular torque do not effect the switching delay.

In a perpendicular free layer, the field like torque only affects the precession of the magnetization and does not affect the switching speed (see Fig. 1.5).

1.3 'First principles' evaluation of TMR and STT

The simple barrier model described in Section 1.2 captures the salient aspects of spin dependent transport. As we can see from Eq. (1.9) the TMR ratio increases as the polarization of the contact increases. However, the free-electron approximation is not always appropriate for real materials with complicated band structures. It is well known, for instance, that large TMR ratios can be achieved in epitaxially-grown crystalline Fe/MgO [27] and CoFeB/MgO [28] MTJs, reaching up to 604% at room temperature and 1144% at 5 K [29, 30] for CoFeB. These large TMR values are attributed to the phase coherent, transverse momentum conserving, transport arising from the energy, orbital and spin dependence of the tunneling matrices. Extensive reviews on the transport properties of crystalline MTJs can be found in Refs. [31] and [32]. In this section we will present a practical scheme for evaluating both the TMR and the STT of crystalline MgO-based MTJs from first principles. We will employ the NEGF approach [33] combined with DFT for the electronic structure description. Our results are obtained with the SMEAGOL code [34, 35], which constitutes a computationally-efficient (order-N) implementation of the NEGF+DFT method.

The ballistic current through the junction is calculated by using the *two-spin-fluid approximation*[36], where the spin-currents for majority ($\uparrow$) and minority ($\downarrow$) spins do not mix. In other words, we ignore spin-flip scattering. We assume periodic boundary conditions in the plane perpendicular to the transport and invoke Bloch's theorem in plane. The total spin-dependent transmission coefficient, $T_\sigma(E;V)$, for electrons at energy E is calculated self-consistently at an applied bias across the junction, V, and integrated to give the net spin current

$$I_\sigma(V) = \frac{e}{h}\int dE T_\sigma(E;V)[f_{\rm L} - f_{\rm R}]\,, \tag{1.22}$$

where $\sigma = \{\uparrow,\downarrow\}$ is the spin index and $f_{\rm L,R}$ are the bias separated Fermi functions of the left and right electrodes, evaluated at $(E - E_{\rm F,L/R})/k_B\mathcal{T}$ (k_B is the Boltzmann constant and $\mathcal{T}$ the temperature). The Fermi energy of the left electrode is given by $E_{\rm F,L} = E_F + eV/2$, and the one of the right electrode by $E_{\rm F,R} = E_F - eV/2$, maintaining a zero average potential across the insulator (we can choose a different voltage convention as long as we consistently include the average drop in the insulator). Here E_F is the Fermi energy of the semi-infinite electrodes at $V = 0$. Translational invariance in the transverse direction allows us to write

$$T_\sigma(E;V) = \frac{1}{\Omega_k}\int d\mathbf{k}_\perp T_\sigma(E,\mathbf{k}_\perp;V)\,, \tag{1.23}$$

where the integral runs over the two-dimensional Brillouin zone (BZ) perpendicular to the transport direction with total area Ω_k. The NEGF formalism yields the

transmission coefficient for each transverse mode $\mathbf{k}_\perp$ as

$$T_\sigma(E,\mathbf{k}_\perp;V) = \mathrm{Tr}\left[\Gamma_{L,\sigma}(E,\mathbf{k}_\perp)G^\dagger(E,\mathbf{k}_\perp)\Gamma_{R,\sigma}(E,\mathbf{k}_\perp)G(E,\mathbf{k}_\perp)\right] . \quad (1.24)$$

Omitting the spin and wave-vector arguments for simplicity, the retarded Green's function $G(E)$ and the electrode-coupling matrices $\Gamma_{\mathrm{L,R}}(E)$ are defined as

$$\begin{aligned} G(E) &= \Big(ES - H - \Sigma_L(E) - \Sigma_R(E)\Big)^{-1}, \\ \Gamma_{L,R}(E) &= i\Big(\Sigma_{L,R}(E) - \Sigma^\dagger_{L,R}(E)\Big), \end{aligned} \quad (1.25)$$

where H is the Kohn-Sham Hamiltonian matrix, S is the overlap matrix, and $\Sigma_{L,R}$ are *self-energy* matrices, which account for the presence of the two semi-infinite crystaline electrodes (leads) [33]. Tunnel junctions typically require large $\mathbf{k}_\perp$ samplings in order to converge $T_\sigma(E;V)$. A 100×100 $\mathbf{k}_\perp$-point mesh is used for the Fe/MgO/Fe junctions discussed in the following section.

1.3.1 The TMR effect in the MgO barrier

1.3.1.1 Symmetry filtering in Fe/MgO/Fe Calculations of the linear response current predict very large TMR for MgO based junctions [18, 37, 38, 39, 40, 41]. The TMR is found to be governed not only by the spin-polarization of the electrode DOS, but also by the details of wave function matching across the barrier. This is analyzed in detail in Ref. [18, 42], where it is shown that the decay of a wave function across the barrier depends mainly on two factors: 1) the specific $\mathbf{k}_\perp$-point in the 2D BZ perpendicular to the transport direction (assumed along z), and 2) the symmetry of the wave function. The bands in Fig. 1.6 summarize the underlying physics. In MgO, states with Δ_1 symmetry at the Γ-point transform like a linear combination of functions with 1, z and $3z^2 - r^2$ symmetry [18] and have no momentum components in the $x - y$ plane. These states share the symmetry of the conduction and valence band edges and thus their complex bands must bend around to connect them, making the corresponding decay constant particularly small when the Fermi energy lies at midgap. Furthermore, the lack of angular momentum components in the $x - y$ plane maximizes their longitudinal energy and thus their decay lengths. In contrast, other midgap states such as Δ_5 created out of zx and zy symmetry, or Δ_2 created out of $x^2 - y^2$ and xy states have much lower longitudinal energies for a given total energy, and do not share the symmetry of the conduction bands. Their complex bands do not need to bend around to connect with the two band edges, making them much less dispersive. We therefore have a strong symmetry filtering, where Δ_1 states decay slowly across MgO but those with Δ_5, Δ_2 and higher in plane angular momentum components decay much faster.

In order to convert symmetry filtering into spin filtering, we need to align the MgO evanescent Fermi energy states with the propagating states in the contacts. For Fe, Co or CoFe electrodes, the hybridization between s-like and $3z^2 - r^2$ states creates a band repulsion and opens a gap. Under these conditions, a metal like Fe

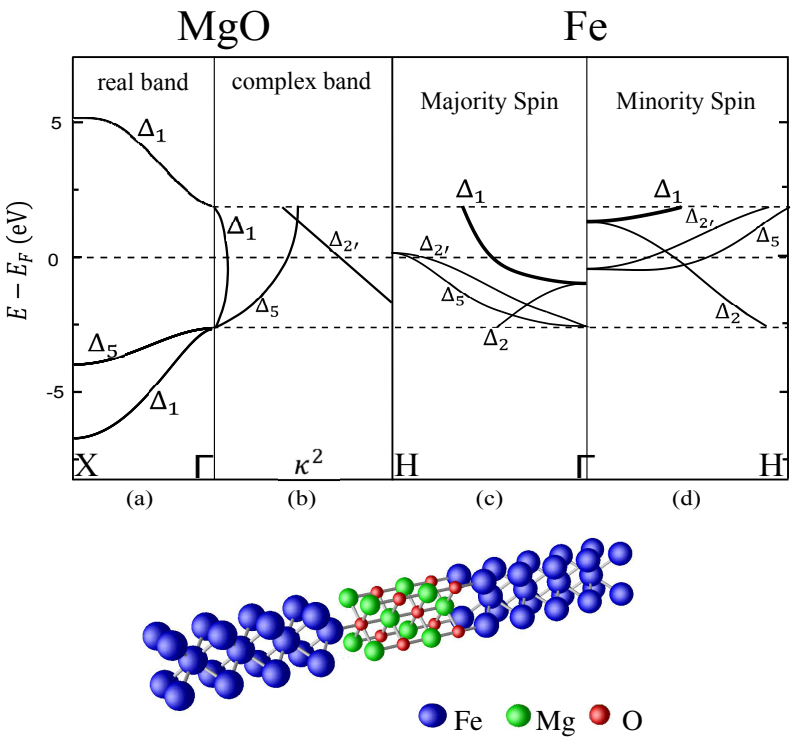

Figure 1.6 (Top) The band origin of spin symmetry filtering. (a) LDA-based band structure and (b) complex band of bulk MgO. The Δ_1 complex evanescent band inside the bandgap of MgO turns around to connect the conduction and the valence band edges with which it shares an overall orbital symmetry. In contrast the Δ_5 and Δ_2' bands have significant angular momentum components perpendicular to the transport axis, so they do not share the band edge symmetry and, as a result, they are non dispersive and strongly decaying. Plotted alongside, (c) Fe enjoys a selective Δ_1 majority spin band crossing the Fermi energy but (d) not one for the minority spin, converting the MgO symmetry filter into an Fe/MgO spin filter. (Bottom) From bulk to heterojunction (color online): unit cell used for the Fe/MgO/Fe(100) junction with 4 MgO MLs. Periodic boundary conditions are applied perpendicular to the stacking direction.

develops a propagating Γ-point Δ_1 band at the Fermi energy only for its majority (↑) spins but not for the minority (Fig. 1.6), leading to a spin selective injection at the Fermi energy. The conjunction of energy placement, spin structure and orbital symmetry implies that Fe electrodes separated by a MgO barrier filter minority spins and effectively behave as half-metals. The corresponding TMR is expected to be very large [18, 37].

MgO is an insulator with NaCl lattice structure, an experimental equilibrium lattice constant of 4.21 Å [43, 44, 45] and a band gap of 7.8 eV [43, 45]. After DFT geometry optimization at the local density approximation (LDA) level, we obtain a

lattice parameter of 4.19 Å, which matches well the experimental value and also previous *ab initio* calculations [46]. The generalised gradient approximation (GGA), in contrast, yields 4.29 Å, i.e. it slightly underbids. In Fig. 1.6 the LDA band structure is shown for the equilibrium lattice constant. We note that the band gap at the Γ point is only 4.64 eV, which is about 3.2 eV smaller than experiments. This discrepancy is caused by the self-interaction error in the LDA exchange correlation potential, but does not change the qualitative features of the problem. Iron is a ferromagnetic metal and crystallizes in the bcc structure, with a room temperature lattice constant of 2.8665 Å [47, 48]. The agreement of the LDA band structure and DOS with the experimental ones is rather good [47, 49].

For bulk bcc Fe we obtain a relaxed lattice constant of 2.79 Å for LDA, and 2.88 Å for GGA, which agrees well with other calculations [50]. The LDA band structure along the Γ-H direction is shown in Fig. 1.7a. This is also in good agreement with other LDA calculations [51] and with experiments [49]. All calculations presented in this section are performed at the LDA level, with the GGA results being rather similar. Minor differences are caused by differences around the Fermi level in the actual band structures obtained with LDA or GGA.

1.3.1.2 Interfacial configuration in Fe/MgO/Fe MTJ Although experimentally the Fe/MgO interface structure depends on the order in which the layers are grown, in all our calculations we use a completely symmetric Fe/MgO/Fe junction. Accordingly, we assume that the Fe electrodes are fixed to their bulk lattice parameters (2.866 Å), while the in-plane MgO lattice adapts perfectly to Fe (lateral periodicity is enforced), making its lattice constant $\sqrt{2} \times 2.866 \approx 4.05$ Å[55].

In Fig.1.6 we show the unit cell of a Fe/MgO/Fe(100) junction with a MgO barrier 4 monolayer (ML) thick. Periodic boundary conditions are applied in the plane perpendicular to the stacking direction. In all our transport calculations, based on the NEGF technique as implemented in the SMEAGOL code, we use 8 Fe layers on each side of the MgO in order to converge to bulk. We construct MgO barriers with an arbitrary number of MLs by using 2.196 Å as the spacing between the MLs. Except for the first interface layer, it is assumed that the Mg and O atoms always have the same z coordinates [39]. A 7×7 $\mathbf{k}_\perp$-points mesh is used during the self-consistent cycle to converge the charge density, while a 100×100 $\mathbf{k}_\perp$-point mesh is used over the full BZ for evaluating the transmission coefficient in a single post-processing step. This finer mesh is necessary in order to resolve sharp resonances in the transmission. We use a real space mesh cutoff of 600 Ry and an electronic temperature of 300 K.

1.3.1.3 Transmission in Fe/MgO/Fe MTJ Let us first analyze the zero-bias energy dependent transmission. Fig. 1.7 shows $T(E; V = 0)$ for the P and AP configurations [panels (b,c)], together with the electronic structure of the Fe leads. In panel (a) we plot the Fe band structure for $k_x = k_y = 0$, while the last three panels show, respectively, the average number of channels, n_c, the bulk DOS, $\mathcal{N}$, and the DOS at

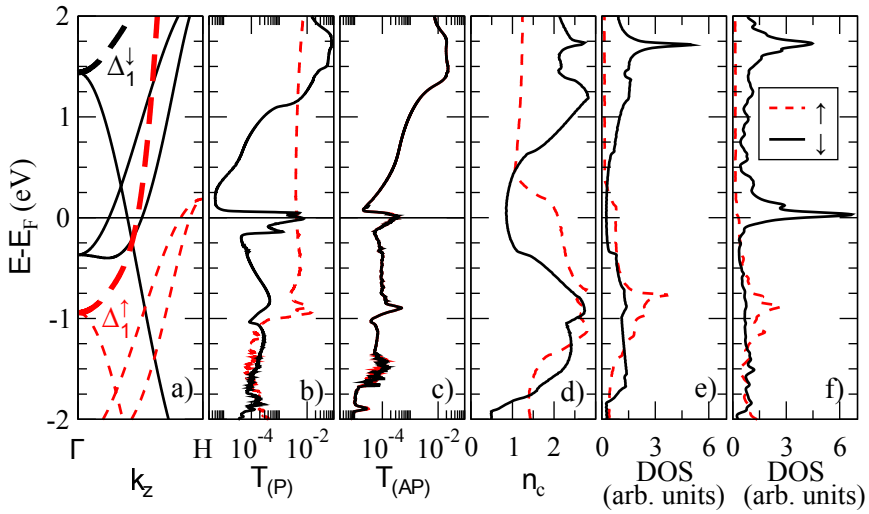

Figure 1.7 (a) Bulk Fe band-structure along the $\Gamma \rightarrow$ H direction (the bands with Δ_1-symmetry are thickened), (b) T_σ in the P configuration, (c) T_σ in the AP configuration, (d) average number of open channels per $\mathbf{k}_\perp$-point for bulk Fe, n_c, (e) bulk Fe DOS and (f) interface Fe-layer DOS, all for both majority and minority spin ($\sigma = \uparrow, \downarrow$). Note that the Δ_1 band-edges coincide approximately with a rather sharp increase in both transmission coefficients $T_{\uparrow,\downarrow}$. Figure reprinted from ref[55] with permission from the authors.

the Fe interface layer for both majority and minority spins. By definition,

$$\mathcal{N} = \frac{1}{\pi \Omega_{BZ}} \int d\mathbf{k}_\perp \sum_i^{N_{\mathbf{k}_\perp}^{(\text{open})}} \frac{1}{v_{\mathbf{k}_\perp,i}} \quad \text{and} \quad n_c = \overline{\mathcal{N} v} = \frac{1}{\pi} \int d\mathbf{k}_\perp N_{\mathbf{k}_\perp}^{(\text{open})}, \quad (1.26)$$

where the integral runs over the 2D BZ perpendicular to the transport direction, $N_{\mathbf{k}_\perp}^{(\text{open})}$ is the number of open channels for a given $\mathbf{k}_\perp$ and $v_{\mathbf{k}_\perp,i}$ is the group velocity for channel i.

For the MTJ P configuration, and for energies in the range of about ± 1 eV around E_F, the transmission for $\uparrow$ spins is much larger than that for the $\downarrow$ spins (note the logarithmic scale). Very close to E_F, however, there is a sharp peak in the minority transmission ($T_\downarrow$), which is due to an interface (IS) state found close to E_F. Below about -1 eV, $T_\uparrow$ drops out as well as this is the energy of the band-edge of the majority Δ_1 state, $\Delta_1^\uparrow$, at the Γ point (see Fig. 1.7a). At this energy we also find a IS in the $\uparrow$ spins, which causes the peak in the transmission. The sharp increase in $T_\downarrow$ at about 1 eV to 1.5 eV is due to the fact that at 1.5 eV there is the band-edge of the minority Δ_1 states, $\Delta_1^\downarrow$, at the Γ point. For other energies inside the MgO band gap the transmission varies, following also the change in the number of channels. An increase in n_c usually is translated in an increased transmission. For energies outside of the MgO band gap the transmission is roughly proportional to the number

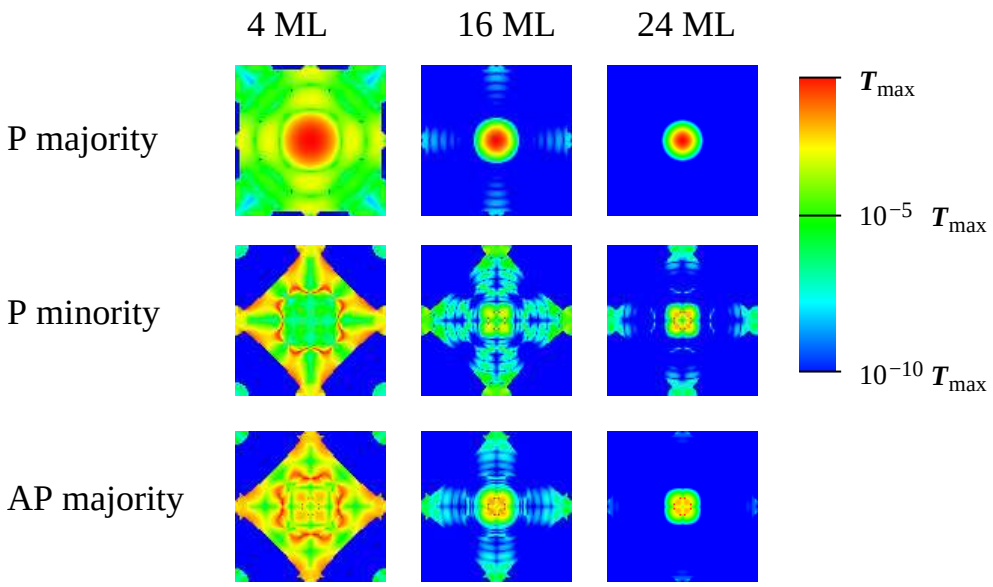

Figure 1.8 (color online) $\mathbf{k}_\perp$-resolved transmission coefficient at $E_{\rm F}$ for the $\uparrow$ and $\downarrow$ spins in the P configuration, and for the $\uparrow$ spins for the AP, for different MgO thicknesses. In each figure a different logarithmic color scale is used, where the red color corresponds to the maximum transmission of each figure, $T_{\max}$, and the blue color corresponds to $10^{-10}\ T_{\max}$.

of channels, with the scattering across the MgO bands leading to some variations. As a first approximation, the transmission in the anti-parallel (AP) configuration can be seen as a convolution of the majority and minority transmission in the parallel one [52, 53]. Around $E_{\rm F}$ it is much lower than the one for the P configuration. The resulting 0-bias TMR is very large, namely 1780%.

In Fig. 1.8 we show the $\mathbf{k}_\perp$-dependent transmission coefficient at $E_{\rm F}$, for $\uparrow$ (first row) and $\downarrow$ (second row) spins in the P configuration, and $\uparrow$ spins in the AP, evaluated for 4, 16 and 24 MgO MLs. The color code is chosen in such a way that for each graph the red color corresponds to the relative maximum transmission. Therefore the red spots indicate in which parts of the BZ the transmission is large. The blue color is chosen to be 10^{-10} times smaller than such maximum value. Hence, the main contributions to the transmission originate only from $\mathbf{k}_\perp$-points close to Γ. The Γ point filtering effect is enhanced when the thickness of the MgO layer is increased.

1.3.1.4 Bias dependent transmission The extension of the calculations to finite bias is critical for extracting both the bias dependence of the TMR, as well as the spin current needed to calculate the STT. Thankfully the self-consistent electrostatic potential is trivial across the junction. The total potential is flat in the metals because of the near complete screening, and it is dominated by the linear Laplace potential across the MgO because of poor screening. Fig. 1.9(a) shows $\Delta V_{\rm H}$, namely the dif-

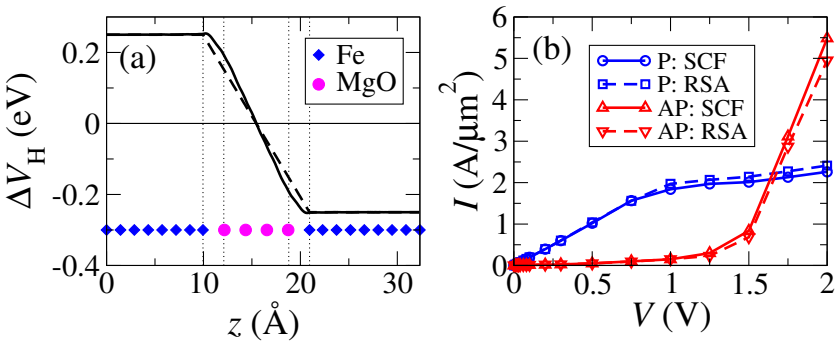

Figure 1.9 (a) Planar average $\Delta V_{\rm H}$ of the difference between the self-consistent Hartree potential at 0.5 V and the one at $V = 0$ (full line). The dashed line indicates $\Delta V_{\rm H}$ applied in the rigid shift approximation. Diamonds and dots indicate the location of the Fe and MgO layers, respectively. (b) Comparison of the I-V curves for the P and AP configurations obtained with the self-consistent solution (solid lines) and with the rigid shift approximation (dashed lines).

ference between the planar average of the self-consistent Hartree potential at finite bias (0.5 V) and that at $V = 0$ along the junction stack (z-axis). $\Delta V_{\rm H}$ decays almost linearly across MgO and it is flat in the electrodes. The dashed line indicates the ideal linear potential drop, which we refer to as the *rigid shift approximation (RSA)*. In the RSA the finite bias transmission coefficient is calculated self-consistently only at $V = 0$, and then modified under finite bias by applying a rigid shift to the electrode DOS and the electrochemical potentials, bridged by a linear ramp inside the MgO [40]. In order to isolate the effect of charging the junction on the transport we compare the I-V curve obtained fully self-consistently against the one obtained with the RSA, Fig. 1.9(b). We find that indeed the I-V is minimally affected by charging, making the rigid shift approximation reasonable for Fe/MgO junctions. It is clear from the currents in the P and AP configurations that the resulting TMR is expected to be high at low biases and then to decrease with bias.

The calculated TMR ratio as a function of V is presented in Fig. 1.10(a), where one can notice a clear non-monotonic behaviour. Firstly, there is a very sharp decrease of the TMR for a narrow voltage region around $V = 0$, followed by an increase. For large voltages the TMR decays monotonically, leading to a peak at about $V = 0.3$ V. The dependence of the TMR on the bias is determined by the I-V characteristics of the P and AP configurations of the MTJ, which in turn can be understood by looking at the evolution of the various transmission coefficients as a function of bias. These quantities are presented in Fig. 1.11 and help us in driving the discussion.

Three main features characterise the evolution of $T(E;V)$ with V. These can be identified from the plot of $T(E;V = 0)$ for the P configuration as: 1) a sharp increase in transmission at around -1 eV for the $\uparrow$ spins, which is mainly determined by the electronic structure of Fe alone and in fact corresponds to the $\uparrow$ spins Δ_1 band edge (peak 1); 2) a similar, although smoother increase in transmission at above

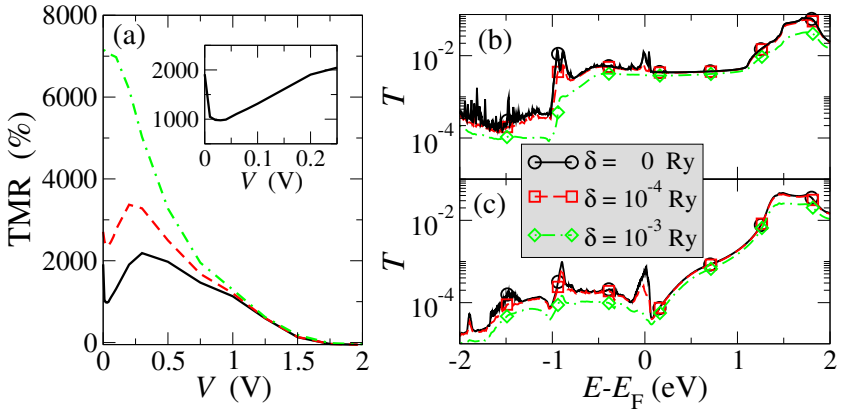

Figure 1.10 (a) TMR as a function of voltage, V. Here δ is an imaginary energy added to the Green's function, which mimics the effects of scattering due to disorder. The black curve is for $\delta = 0$, the red for $\delta = 10^{-4}$ Ry, and the green for $\delta = 10^{-3}$ Ry. In the inset the TMR is shown in the low-bias region for $\delta = 0$.. $T(E; V = 0)$ for different values of δ for the P (b) and the AP (c) configuration. Figure reprinted from ref [55] with permission from the authors.

+1 eV for the $\downarrow$ spins (peak 2), which corresponds to the $\downarrow$ spins Δ_1 band edge; 3) a sharp resonance at $E_{\rm F}$ for the $\downarrow$ spins (peak 3), which is attributed to the presence of a transport resonance across $\downarrow$ spins surface states localised at the two interfaces between Fe and MgO.

As a voltage is applied to the junction the minority resonance at $E_{\rm F}$ for the P configuration splits into two much smaller peaks and the transmission drops drastically. This is because the surface state at the two sides of the junction drift in energy in opposite directions and the resonant condition is lost. Such resonant condition is not present for the AP configuration, since minority spins at one electrode tunnel into the majority ones at the opposite electrode and viceversa. It is such drastic reduction of the transmission in the minority channel of the P configuration that yields to the reduction in TMR at low bias. Note that such reduction occurs on a voltage scale of the order of 20 mV, which is comparable with the natural width of the surface states.

As the bias continues to increase the transmission for the P configuration becomes entirely dominated by the $\uparrow$ spin channel, for which $T(E; V)$ is constant in energy over the bias window. This produces a linear I-V curve, which saturates as soon as the Δ_1 majority band edge enters the bias window. In contrast the transmission for the AP configuration remains small in the bias window up to relatively large voltages. Then, for one of the two spin channels (in the AP case the spin channels are defined with respect to one of the two electrodes) the majority spin Δ_1 band edge of one of the two electrodes starts to overlap in energy with the minority Δ_1 band edge of the other electrode, causing a drastic enhancement of the transmission coefficient and thus of the current. This is the point where the currents for the P and AP configurations start to be similar and consequently the TMR ratio decays.

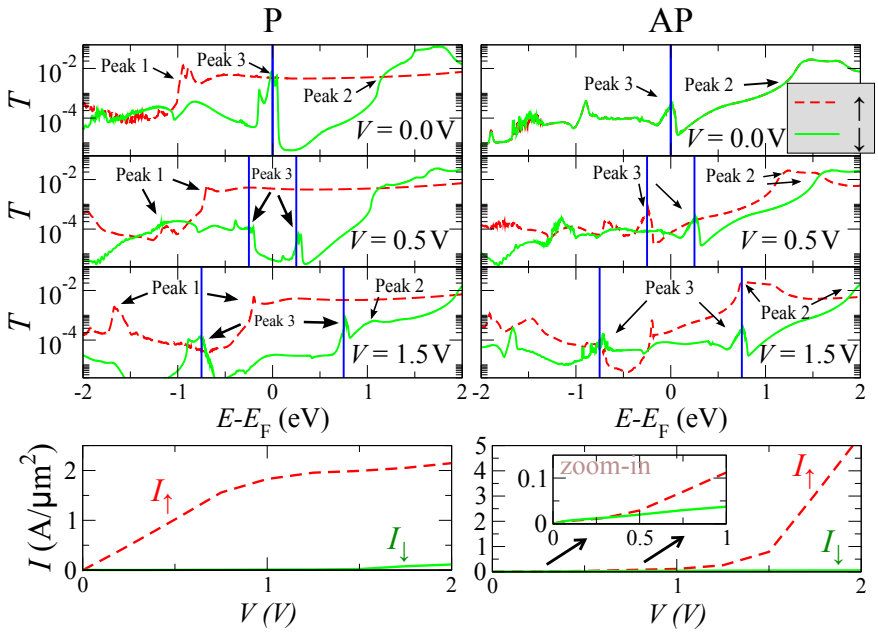

Figure 1.11 Spin-dependent transmission coefficient, $T(E;V)$, as a function of energy, E, and for different biases, V, for the P (left-hand side panels) and for the AP configuration (right hand side panels). The vertical lines are placed at $E = E_{\rm F} \pm eV/2$ and enclose the bias window. Figure reprinted from ref [55] with permission from the authors.

In the analysis presented so far we have considered phase-coherent transport across a perfectly crystalline junction, a situation that typically does not correspond to an actual experiment [54]. Unstructured disorder can be introduced in the calculation of the transmission coefficients by simply adding a small imaginary component δ to the energy when evaluating the Green's function. The effect of such imaginary energy is that of broadening the resonances in the transmission, i.e. in reducing the life-time of the various surface states. This has the effect of smoothing the transmission function as it can be appreciated in Fig. 1.10. The consequence on the TMR of such broadening depends on the details of the junction. In the case investigated here the low-bias non-monotonic dependence of the TMR ratio is washed away and at $\delta = 10^{-3}$ Ry the TMR decreases monotonically across the entire bias range. Notably the low-bias TMR is significantly larger for large δ, while it is not sensitive to the broadening for large voltages, since in this case the I-V curve is dominated by the relative position of the Δ_1 band edges and not by surface states. A monotonic decay of the TMR bias is what commonly observed in experiments for high-quality junctions [27].

The calculations presented here predict a TMR significantly higher than the one typically measured experimentally, which rarely exceeds a few hundred percent [27, 28]. This is consistent with other calculations [18, 38, 40, 39]. It has been shown,

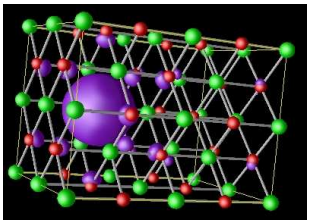

Figure 1.12 (color online) Isosurface of the local DOS of the V_O defect band (purple color); red spheres represent O atoms, and green spheres represent Mg atoms.

however, that oxidation of the interface Fe layers can lead to a drastic reduction of the TMR, which can even become negative for asymmetric oxidation of the electrodes [56, 40, 41, 57]. In Ref. [27] it is noted that lattice dislocations are found at the Fe/MgO interface. These also can lead to a reduction of the TMR. Another possible mechanism leading to a reduction of the TMR is the presence of defects in the MgO, and at the Fe/MgO interface. Calculations for a Fe/vacuum/Fe junction indicate that disorder at the interface can drastically reduce the TMR [58], in agreement with the results of Ref. [57] for a disordered and randomly oxidized Fe/MgO/Fe junction. Experimental results indicate that the density of defects in MgO depends on the growth conditions [59, 60, 61]. Such a large defect density is found to lead to an effectively reduced MgO band gap [60, 61]. In Ref. [60] it is shown that by annealing the sample the band gap opens to the bulk MgO value, indicating that the density of defects is reduced. Measurements of isolated defects indicate a defect level close to the valence band, which is tentatively attributed to Mg vacancies (V_{Mg}), and a set of levels between the E_F and the conduction band, attributed to oxygen vacancies (V_O). The authors note, however, that this correspondence is not completely established at this stage. In Ref. [61] a detailed study of the possible defects in MgO, grown on an Ag substrate have been presented. They find different possible defects, with energies spread over large part of the MgO band gap. One of the defects identified is V_O, whose energy lies approximately in the middle of the MgO band gap. This agrees well with other theoretical predictions [62, 63, 64]. *Ab initio* calculations with Fe/MgO/Fe junctions in Refs. [65, 66] show that for V_O LDA predicts a defect band centered about 1 eV below the Fe Fermi energy. In Ref. [67] experimental evidence is shown on the decrease of the TMR with V_O, supported by a theoretical model.

1.3.1.5 Interfacial defects: Oxygen vacancy In order to investigate the bias dependent influence of defects on the transport, we perform calculations with a V_O inserted within MgO (Fig. 1.12). We find that such a defect has an s-type symmetry (consequently contributes to Δ_1 symmetry bands) and lies very close to the Fe Fermi energy, in good agreement with the results of previous calculations [65, 66]. It is thus indicative of all defects that lead to a small additional DOS in the vicinity of E_F. The exact theoretical description of defects in MgO is a complex task; for instance, it should include a relaxation of the lattice for all defects. Moreover, not all

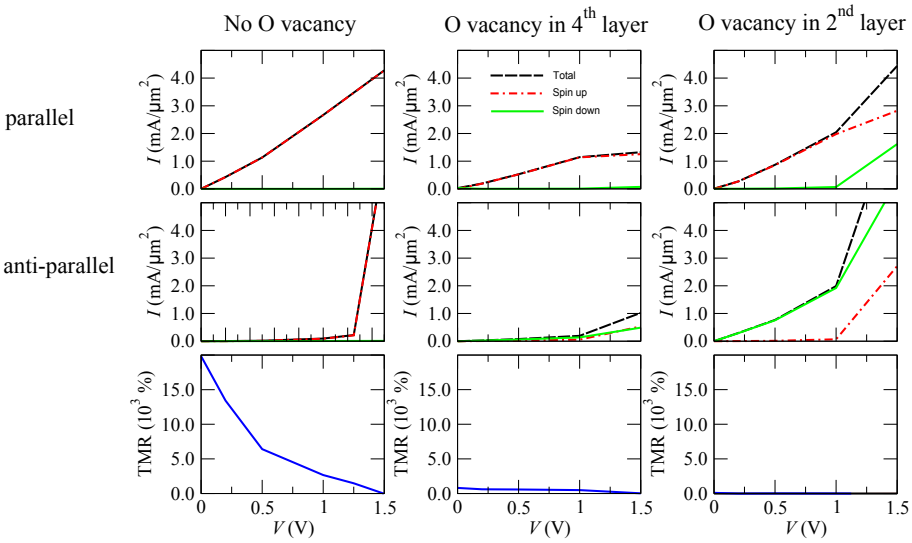

Figure 1.13 Role of oxygen vacancy on tunnel magnetoresistance. The figure shows the spin-polarized current, I, for the P (top row of figures) and the AP alignment (middle row of figures) of the Fe electrodes, as well as the resulting TMR (bottom row of figures). In the plots for the current the red curves correspond to the $\uparrow$ current, the green curves the $\downarrow$ current, and the black curves to the total current. The results are for 8 MLs of MgO with no V_O (leftmost panels), with a V_O in the forth layer from the interface (middle panels), and with a V_O in the second layer from the interface (rightmost panels).

defects can be described accurately with DFT. However, previous calculations show that DFT can accurately predict the properties of V_O's [62, 63, 64].

In order to keep the size of the calculations tractable, we use a rather high V_O density. We construct a 2×2 supercell in the plane perpendicular to the transport direction. The V_O is then obtained by removing one O atom in one of the MgO MLs. The planar V_O density is therefore 1/4, the total defect density for a 4 MLs junction is 1/16, for a 8 MLs it is 1/32. In all the calculations in this section we do not relax the structure around the defect, and for the Fe/MgO junction we use the unrelaxed coordinates (Ref. [18]). We note that in our calculations the V_O is in a charge neutral state, whereas experimentally the vacancy can exist in different charging states. The presence of a V_O leads to a defect band lying approximately in the middle of the gap (not shown here). Importantly, this defect level is not spin-split. The band shows a rather large dispersion, which is due to the high in-plane defect density.

The bias dependence of the TMR is calculated for a defect-free and for two defective 8 ML junctions: one where the V_O is located in the second ML, and one where it is located in the forth ML from the Fe/MgO interface (Fig. 1.13). We find that the main effect of the vacancies is to enhance the AP current. The closer the vacancy is to the Fe/MgO interface, the stronger is the enhancement. In contrast, a V_O does

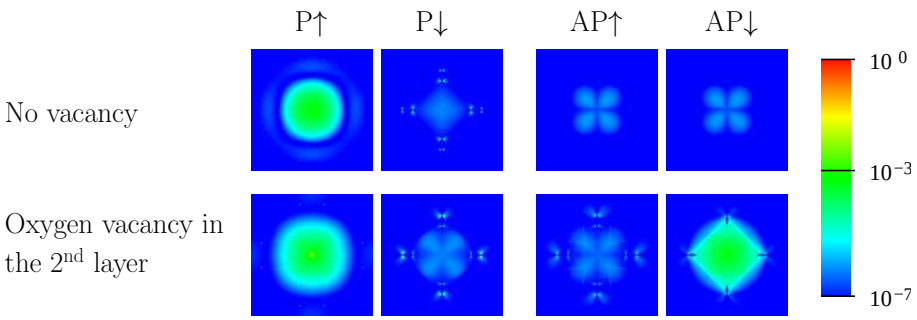

Figure 1.14 (color online) $\mathbf{k}_\perp$-dependent transmission for P↑ (first column), P↓ (second column), AP↑ (third column), and AP↓ (fourth column), at an energy $E - E_F = -0.2$ eV. The first row of figures is for an ideal 8 MgO MLs junction, the second row is for a junction with a V_O in the second MgO layer from the interface.

not lead to a significant change of the P current, although there are some quantitative differences with respect to the defect-free case. Overall we see that the TMR is drastically reduced in the junctions containing the V_O's, and basically vanishes if the vacancy is at or closer to the interface than the second ML.

Clues for the enhanced AP transmission in the defective junctions can be found in the $\mathbf{k}_\perp$-dependent transmission presented in Fig. 1.14 for the ideal junction, and for the 8 ML junction with the V_O in the second ML. The plot shows $T(\mathbf{k}_\perp)$ at an energy of -0.2 eV below E_F. This is lower than the lowest energy of the surface state, and lies in the region of high transmission for the AP configuration in the defective junctions. For the ideal junction the transmission is highest for the P ↑ states, since in that case there is a large density of the high-transmission Δ_1-like states on both sides of the junction. For the P ↓ the contribution of the Δ_1 like states on both sides of the junction is rather small, and the transmission is correspondingly reduced. In the AP configuration the transmission is identical for ↑ and ↓, as the perfect junction is completely symmetric. Since on one side there is a high density of Δ_1 states, whereas on the other side the density is low, the transmission is much smaller than for P ↑, but somewhat larger than for P ↓.

For the junction with the V_O in the second ML, the situation is very different. Since the vacancy is not spin-polarized, the electrons flowing through the vacancy states at this energy have approximately the same density of Δ_1 states for both ↑ and ↓. On the left side of the junction to which the V_O is very close, there is a large Δ_1 DOS for both ↑ and ↓. On the right side and for P configuration, the ↑ has a much larger contribution from the Δ_1 states than the ↓, so that the P ↑ transmission is similar to the one of the ideal junction, whereas the P ↓ transmission is similar to the one of the ideal junction for AP alignment. For AP alignment of the defective junction the situation is reversed, and the larger transmission comes from the ↓, and is similar in size to the P ↑ transmission. The AP ↑ transmission on the other hand is similar in size to the AP transmission for the ideal junction. *We therefore conclude*

that the enhancement in transmission in the AP configuration in a defective junction is caused by the depolarization of the Δ_1 states at the vacancy site. If this sits very close to the Fe/MgO interface, it effectively leads to a depolarization at the interface. If the vacancy lies in the middle of the junction, the effect is less pronounced, since the states need to tunnel to the vacancy site from both interfaces, where the Δ_1 DOS is small. However the TMR is reduced in this case as well. Our *ab initio* result agrees qualitatively with the conclusions of Ref. [67].

1.3.2 Currents and torques in NEGF

After the extensive discussion on the TMR characterizing the read operation, let us now move on to the spin torque relevant for the write operation. As outlined in Sec. 1.2, the torque acting on a magnetic layer can be obtained by evaluating the difference in spin currents on the left and right of this layer. We formulate the general NEGF based formalism for evaluating such spin-currents in non-collinear systems from first principles. The NEGF Hamiltonian is obtained either from DFT or else from an empirical tight-binding (TB) model, projected over a localized orbitals basis set. The so obtained single particle Hamiltonian, H, and the density matrix, ρ, can be written as a sum of a spin-dependent part and spin-independent part

$$\begin{aligned} H &= H_0 \cdot \mathbb{I} + \vec{H}_{\mathrm{S}} \cdot \vec{\sigma} \\ \rho &= \rho_0 \cdot \mathbb{I} + \vec{\rho}_{\mathrm{S}} \cdot \vec{\sigma} \end{aligned} \tag{1.27}$$

where $\vec{\sigma} = (\sigma_x, \sigma_y, \sigma_z)$, with $\sigma_x, \sigma_y, \sigma_z$ the three Pauli matrices, and $\mathbb{I}$ is the 2×2 unity matrix. H_0 is the spin-independent part of H, while $\vec{H}_{\mathrm{S}} = (H_x, H_y, H_z)$ represents the spin-components of H corresponding to the exchange field. In the same way ρ_0 is split into its spin-independent part ρ_0 and its spin-vector $\vec{\rho}_S = (\rho_x, \rho_y, \rho_z)$. Note that H_α and ρ_α, with $\alpha \in \{0, x, y, z\}$, are $N_{\mathrm{o}} \times N_{\mathrm{o}}$ matrices, with N_{o} being the number of orbitals in the simulation cell.

Using $G, \Gamma_{\mathrm{L,R}}$ and $f_{\mathrm{L,R}}$ introduced in section 1.3, we can define the lesser Green's function, $G^<(E)$, as

$$G^<(E) = iG\Gamma_L G^\dagger f_L + iG\Gamma_R G^\dagger f_R. \tag{1.28}$$

Analogous to H and ρ we can split $G^<(E)$ into its spin components

$$G^<(E) = G_0^<(E) \cdot \mathrm{I} + \vec{G}_{\mathrm{S}}^<(E) \cdot \vec{\sigma}, \tag{1.29}$$

with $\vec{G}_{\mathrm{S}}^<(E) = \big(G_x^<(E), G_y^<(E), G_z^<(E)\big)$. The density matrix is then related to $G^<(E)$ by

$$\rho = \frac{1}{2\pi i} \int_{-\infty}^{\infty} G^<(E) dE. \tag{1.30}$$

In Sec. 1.3 we introduced $T(E)$ as the total energy dependent transmission from left to right electrode. We can in addition evaluate the charge and spin current resolved between any two orbitals i and j in the system. This is denoted as

the bond current J_{ij}[68], and can be separated in its spin components $J_{ij}(E) = J_{e,ij}(E) \cdot \mathbb{I} + \vec{J}_{\mathrm{S},ij}(E) \cdot \vec{\sigma}$, with $\vec{J}_{\mathrm{S},ij}(E) = (J_{x,ij}(E), J_{y,ij}(E), J_{z,ij}(E))$, and the energy dependent electron current $J_{e,ij}(E)$. Within the NEGF formalism, and for systems with general overlap matrix S (of dimension $N_\mathrm{o} \times N_\mathrm{o}$), the spin-dependent bond current is given by

$$\begin{aligned} J_{e,ij}(E) &= \frac{4e}{h}\Re\left[(H_{0,ij} - ES_{ij})G^<_{0,ji}(E) + H_{x,ij}G^<_{x,ji}(E)\right. \\ &\qquad \left. + H_{y,ij}G^<_{y,ji}(E) + H_{z,ij}G^<_{z,ji}(E)\right] \\ J_{\alpha,ij}(E) &= \frac{4e}{h}\Re\left[H_{\alpha,ij}G^<_{0,ji}(E) + (H_{0,ij} - ES_{ij})\,G^<_{\alpha,ji}(E)\right], \end{aligned} \tag{1.31}$$

with $\alpha \in \{x, y, z\}$, and $\Re$ denotes the real part. The total spin current is obtained by integrating over all energies, and results to

$$\begin{aligned} I_{e,ij} &= -\frac{4e}{\hbar}\Im\left[H_{0,ij}\rho_{0,ji} - S_{ij}F_{0,ji} + H_{x,ij}\rho_{x,ji} + H_{y,ij}\rho_{y,ji} + H_{z,ij}\rho_{z,ji}\right] \\ I_{\alpha,ij} &= -\frac{4e}{\hbar}\Im\left[H_{\alpha,ij}\rho_{0,ji} + (H_{0,ij}\rho_{\alpha,ji} - S_{ij}F_{\alpha,ji})\right], \end{aligned} \tag{1.32}$$

with $\alpha \in \{x, y, z\}$, and $\Im$ denotes the imaginary part. Here we have introduced the energy density matrix, F, which is given by[69]

$$F = \frac{1}{2\pi i}\int_{-\infty}^{\infty} EG^<(E)dE \tag{1.33}$$

In order to obtain the current from a subsystem, denoted as SS_1, to another subsystem, denoted as SS_2, one needs to sum over all the possible orbital-to-orbital currents

$$I_{\alpha,SS_1,SS_2} = \sum_{i\in SS_1}\sum_{j\in SS_2} I_{\alpha,ij}, \tag{1.34}$$

with $\alpha \in \{e, x, y, z\}$. In a layered system such as typical MTJs, we can evaluate the current across different layers. We denote as $I_{\alpha,n}$ the current across a layer with index n in our cell, so that SS_1 includes all orbitals with centers on or to the left of layer n, while SS_2 includes all orbitals with centers to the righ of layer n. As discussed in Sec. 1.2 we can evaluate the total STT on any sub-system by evaluating the difference of the incoming and outgoing spin current to/from the sub-system. This is in line with the STT definition originally proposed for MTJs by Slonczewski [21], based on the conservation of spin angular momentum and the free-electron Bardeen theory for the tunneling current. The first NEGF-based formulation of Slonczewski's STT definition was proposed by Theodonis et al. [70]. More recently, other works [71] focus on deriving approximate expressions for the STT involving only collinear NEGF characteristics.

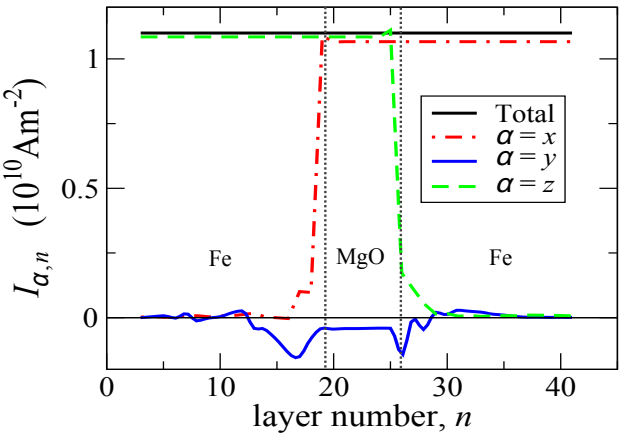

Figure 1.15 Layer-resolved spin current at 0.5 V for a Fe/MgO/Fe junction, with the layer index denoted by n ($n \in [1, 19]$ correspond to the Fe layers in the left electrode, $n \in [20, 25]$ are the MgO monolayers, and $n \in [26, 41]$ correspond to the Fe layers in the right electrode).

1.3.3 First principles results on spin transfer torque

Ab-initio calculations of spin transfer torque habe been performed for various junctions[72, 73, 74]. We evaluate the STT for a the defect-free Fe/MgO/Fe tunnel junctions introduced in Sec. 1.3.1. Here we use 6 MgO monolayers, so that the interface state contribution to the current is suppressed. In Fig. 1.15 the layer resolved spin-current is shown for the different layers in our simulation cell. We apply the bias voltage non-selfconsistently within the RSA, since it gives a good approximation for the current when compared to the fully self-consistent solution (see Fig. 1.9). The bias voltage corresponds to 0.5 V, and the magnetic moment of the left electrode is along the z direction, while the one for the right electrode is along the x direction. We see that the current is fully polarized along z (x) deep in the left (right) electrode, showing that the local spin-current is parallel to the magnetization in the electrode. A torque is exerted at the layer index n where $I_{\alpha,n}$ changes significantly. We see that the torque is localized mainly at the Fe/MgO interfaces. For example, $I_{z,n}$ drops from its left-electrode bulk value to approximately 0 within the first 4 Fe layers of the right electrode, which implies that the total torque along z (the in-plane torque for the right electrode) acts within these first 4 Fe layers. The out-of plane torque is determined by the y components of the spin-current, and acts also mostly close to the MgO/Fe interfaces, although it protrudes deeper into the electrodes. Importantly, we note that the total electron current is constant over the whole system.

In the remaining part of this subsection we consider the total torque acting on the right electrode, which is simply given by the spin-currents along z (y) in the middle of the MgO spacer for the in-plane (out-of-plane) torque, since the total spin-current deep in the right electrode is fully polarized along the x direction (see Fig. 1.16).

Fig. 1.17 shows the first principles torque. As discussed earlier, the low bias current driven STT is linear in V while the field like STT is quadratic in V, with a small non zero component even at equilibrium. This small $V = 0$ out-of-plane torque is due to the exchange interaction between the left and right Fe electrodes across the MgO. At high bias above ~ 1.5 V the torque shows a highly non-monotonic behavior and can also change sign. This is due to the fact that at these high voltages the current in the anti-parallel configuration increases rapidly and eventually becomes larger than the one for parallel alignment (see Fig. 1.13 for the 8 MgO monolayer junction).

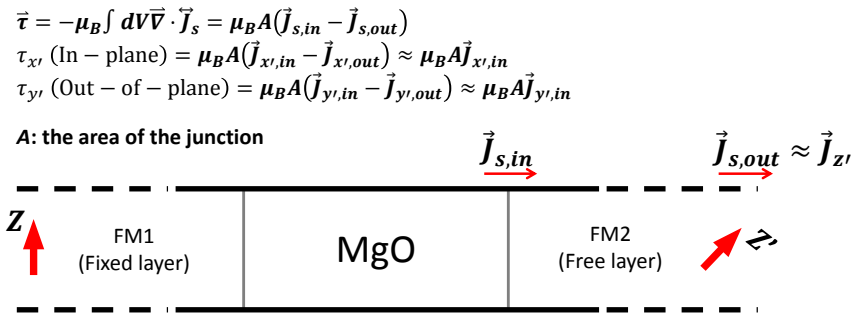

Figure 1.16 Schematic of the definition of the STT at the right-hand-side electrode through spin-current fluxes.

In the literature the total electron density is often split into a "condensate" or "equilibrium part" (EP), and a "non-equilibrium part" (NEP) [34]. Within NEGF the EP is usually written as

$$\rho_{\mathrm{EP}} = \frac{1}{2\pi i} \int_{-\infty}^{\infty} (-1) \left(G(E) - G^{\dagger}(E)\right) \left[\xi f_{\mathrm{R}} + (1-\xi) f_{\mathrm{L}}\right] dE, \tag{1.35}$$

and the NEP as

$$\rho_{\mathrm{NEP}} = \frac{1}{2\pi i} \int_{-\infty}^{\infty} iG(E) \left[\xi \Gamma_{\mathrm{L}} - (1-\xi)\Gamma_{\mathrm{R}}\right] G^{\dagger}(E) \left(f_{\mathrm{L}} - f_{\mathrm{R}}\right) dE, \tag{1.36}$$

with $\xi \in [0,1]$, so that $\rho = \rho_{\mathrm{EP}} + \rho_{\mathrm{NEP}}$. Such a partitioning is not physically motivated and the choice of the terms 'equilibrium' and 'nonequilibrium' is somewhat of a misnomer. The true 'equilibrium part' would correspond to $f_{\mathrm{L}} = f_{\mathrm{R}}$ and the partitioning thereafter would not be arbitrary, provided the voltage division among the contacts is consistent with the intermediate Laplace potential matching all boundary conditions. The drive to make the EP and NEP division is primarily computational, since the so-called EP part in Eq. 1.35 involves just the imaginary part of G, whose poles are localized entirely in one half of the complex energy plane. The simple pole structure makes the corresponding EP integral easy to evaluate on a contour, leaving

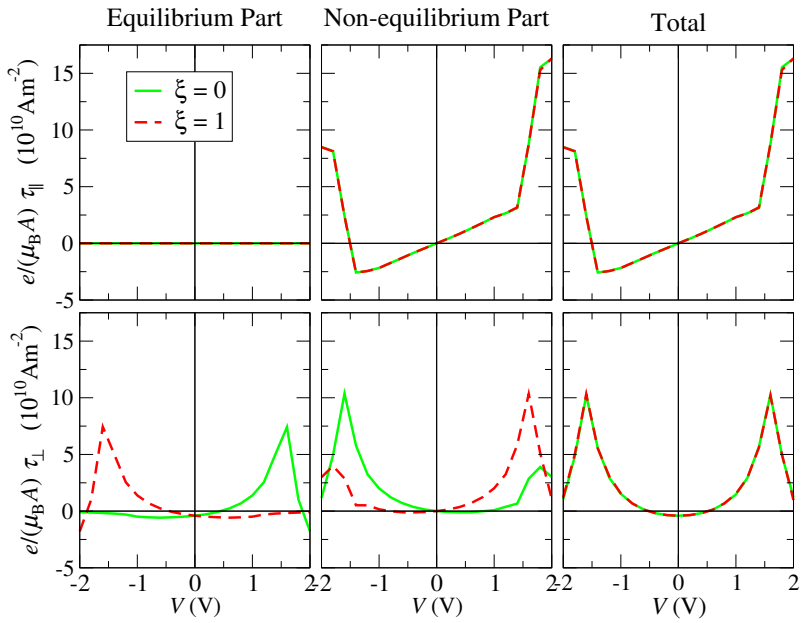

Figure 1.17 Bias dependence of the 'equilibrium' and 'non-equilibrium' components (defined in the text) of the in and out of plane components of STT for a Fe/MgO/Fe junction with 6 MgO monolayers, with ξ defined in Eqs. (1.35) and (1.36).

just an energy window over which the residual NEP integral needs to be computed brute force. Since ξ can be chosen arbitarily in the range from 0 to 1, the splitting in EP and NEP is not unique. In the same way the energy density is split into EP and NEP. The EP of the torque is then obtained by using ρ_{EP} and F_{EP} in Eq. (1.32), while the NEP torque is obtained by using ρ_{NEP} and F_{NEP}, so that the total torque is the sum of EP and NEP torques. The results are shown in Fig. 1.17 for $\xi = 0$ and $\xi = 1$. While the in-plane torque is identical for any choice of ξ, it can be seen that the individual out-of-plane components change completely depending on the choice of ξ. Importantly, the total out-of-plane torque is independent of the choice of ξ, indicating that *the only meaningful quantity is the total torque*, and it is not really meaningful to split it into the arbitrary EP and NEP parts.

We conclude this subsection by presenting the dependence of the torque on the electrode composition. Typically a mixture of Co and Fe is used as electrodes [75]. We consider 4 different systems here: 1) Fe-MgO-Fe is the system considered so far, 2) Co-MgO-Co is the system where we replace the Fe atoms with Co atoms, 3) CoFe-MgO-FeCo is a system where we put alternating layers of Fe and Co, and where a Fe atom is placed at the interface to MgO on both sides, 4) FeCo-MgO-CoFe is the same as system 3), but where we put a Co atom at both interfaces to MgO. The resulting torque data are shown in Fig. 1.18. The general trends are similar for all junctions, but there are significant quantitative differences. For the Co-MgO-Co

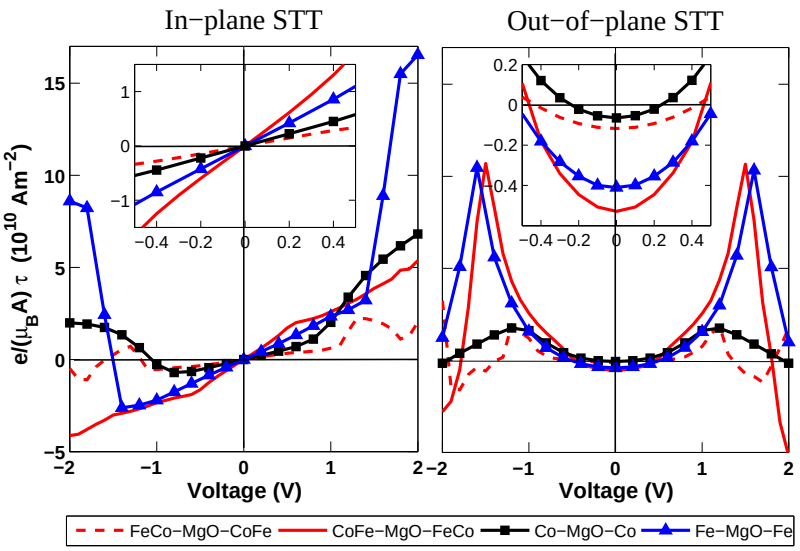

Figure 1.18 Comparison of in-plane and out-of-plane STT for different electrode compositions.

junction we find the onset of the non-linear behavior for the in-plane torque already at about 1 V. The early onset of nonlinearity arises from the fact that Co has one more electron than Fe, so that the Fermi energy is effectively shifted to higher energies. For the mixed systems we see that the metal layer adjacent to the MgO is of key importance: CoFe-MgO-FeCo shows the highest low-bias torque, while FeCo-MgO-CoFe shows the smallest one. For randomly mixed FeCo systems we expect that the overall torque corresponds to some average of the shown results, although clearly the local torque will still be strongly dependent on the vicinal atomic structure. DFT based calculations are the only practical means to evaluate the material and bias-dependent variations in the STT for realistic interfaces. The microscopic insights and physical understanding we drawn from these simulations are of clear significance to the development of STT-MRAM technology.

1.4 Magnetization dynamics

1.4.1 Landau-Lifshitz-Gilbert equation

To generate a complete description of magnetization dynamics under the action of a spin transfer torque, we need to go beyond atomic bandstructure to broader magnetic parameters such as the geometry of magnet, magnetic anisotropy and damping. We use the Landau-Lifshitz-Gilbert (LLG) equation to describe the precessional motion of magnetization under various torques. For a nano size magnet such as the free layer

in STT-MRAM, a single domain is often energetically favorable and the magnetization switching $\vec{M}(t)$ can be determined by the normalized LLG equation,

$$\frac{d\vec{m}}{dt} = -\gamma\vec{m} \times \vec{H}_{eff} + \alpha\left(\vec{m} \times \frac{d\vec{m}}{dt}\right) \tag{1.37}$$

with $\vec{m} = \vec{M}/M_s$ the unit vector along the magnetization direction, M_s the saturation magnetization (kept constant during the switching), α the damping constant, γ the electron gyromagnetic ratio (2.21×10^5 rad $\cdot$ m/A $\cdot$ s) and $\vec{H}_{eff}$ the effective magnetic field contributing to the precessional torque (first term to the right of Eq. 1.37)

$$\vec{H}_{eff} = -\frac{1}{\mu_0\Omega}\frac{dE}{d\vec{M}} \tag{1.38}$$

Here μ_0 is the vacuum permeability, Ω is the volume of the magnet and E is the total free energy at zero temperature, bearing contributions from both the demagnetization field and the external magnetic field $E = E_{demag} + E_{ext}$. The second term in Eq. 1.37 acts as a 'viscous' force that dissipates the kinetic energy and tends to drive the magnetization back to its equilibrium position. To include the destabilizing spin transfer torque that we calculated in the previous sections, we need to add extra torque terms $\vec{\tau}_s = \vec{\tau}_{||} + \vec{\tau}_{\perp}$ in Eq 1.37 where $\vec{\tau}_{||} = a(V)\vec{m} \times (\vec{m} \times \vec{m}_s)$ and $\vec{\tau}_{\perp} = b(V)\,(\vec{m} \times \vec{m}_s)$ with $a(V), b(V)$ being the bias dependent factors (quasilinear and quadratic in V) that we outlined in section 1.2.1.3 and plotted in Fig. 1.18

$$\begin{aligned}\frac{d\vec{m}}{dt} =& -\gamma\vec{m} \times \vec{H}_{eff} + \alpha\left(\vec{m} \times \frac{d\vec{m}}{dt}\right) \\ & - a(V)\vec{m} \times (\vec{m} \times \vec{m}_s) - b(V)\,(\vec{m} \times \vec{m}_s)\end{aligned} \tag{1.39}$$

We have been referring to $\vec{\tau}_{\perp}$ as the 'field-like' torque because it resembles the magnetic field induced torque in the LLG equation, or the 'perpendicular' torque since $\vec{\tau}_{\perp} \perp \vec{m}, \vec{m}_s$. We refer to the other torque $\vec{\tau}_{||}$ as the 'Slonczewski' torque or 'in-plane' torque. $\vec{\tau}_{||}$ is similar in form to the damping term in LLG, but instead of pulling back the magnetization to the easy axis it drives it into alignment with the incoming spin $\vec{m}_s$. The competing components in the LLG equation are shown schematically in figure 1.19.

The above LLG equation can be solved by numerical integration given $a(V)$ and $b(V)$. From the previous section on ab-initio STT, we find that $a(V), b(V)$ in general have complicated dependences on bias, but at low voltage $a(V)$ is quasilinear and can be approximated as $a(V) \approx \mu_B I\eta/e\Omega M_s$, where η is the polarization and I is the charge current (recall eq 1.12). Since $b(V) \propto V^2$ and because the field-like term induces magnetization precession rather than switching, it is often neglected in the analytical solution. By balancing the spin transfer torque and the magnetic damping at small initial angle, the critical switching current and switching time for AP-to-P switching is obtained by J.Z.Sun for an in-plane uni-axial MTJ for small angles[77]

$$I_{c0} = \frac{2\alpha e}{\eta\hbar}\mu_0 M_s \Omega H_k \left(1 + \frac{M_s}{2H_k}\right) \tag{1.40}$$

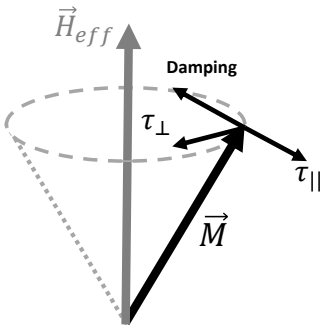

Figure 1.19 Different torques in LLG equation. The field like torque creates magnetization precession. The damping term restores the magnetization to its equilibrium posistion while the Slonczewski torque tries to align the magnetization with incoming electron spins (not shown, anti-parallel to H_{eff} in this figure).

$$t^{-1} = \frac{\alpha\gamma}{\ln(\pi/2\theta_0)}(H_k + \frac{M_s}{2})\left[\left(\frac{I}{I_{c0}}\right) - 1\right], \quad (I > I_{C0}) \tag{1.41}$$

with H_k the uni-axial anisotropy field and θ_0 the initial angle between the magnetizations of the free layer and the fixed layer. For perpendicular MTJ the equations are similar except the demagnetization field M_s now is collinear to H_k and should be included as a correction to H_k. In other words, simply replacing $H_k + M_s/2$ with $H_k - M_s$, we get the equations for perpendicular MTJ. I_{c0} is the minimal current needed to start switching the free layer. Note that the switching time depends on the initial angle θ_0 and the actual overdrive current $I > I_{c0}$. When $\theta_0 \to 0$, $t \to \infty$, which corresponds to the case where the fixed layer and the free layer have strictly parallel magnetization. Such orientations are called 'stagnation points' and ultimately determine the write error rate where the magnetization refuses to switch under an applied bias. The reason for such a stagnation is that the incoming electrons only deposit the angular momentum perpendicular to the magnetization of the free layer, proportional to $\vec{m} \times \vec{m}_s$. A strict parallel or anti-parallel configuration cannot induce torque on the magnetization, so that the switching time is very long when the initial angle is small. Ways to initiate the switching, for instance using a small magnetic field, form topics of research in STT-RAMs. In most experiments, switching happens because of thermal fluctuation which nudges the magnetization from its stagnation point whereupon the current driven torque takes over.

1.4.2 Switching with spin torque in presence of thermal fluctuations

Using our multiscale predictive model coupling DFT+NEGF+LLG, we can now show real-time simulations of switching in the free layer. As discussed earlier, the switching bears an inherent symmetry, in that both AP-to-P and P-to-AP switching occur simply when the density in one spin channel overcomes the other. The difference is that for AP-to-P switching the majority spin is injected from the fixed layer and accumulate at the free layer, while in P-to-AP switching the majority spin is removed from the free layer, effectively building up the local minority spin population.

Fig. 1.20 shows the local electron populations in the various spin channels to illustrate this point. The STT-RAM model under study is fitted with a published experiment for in-plane CoFeB/MgO/CoFeB MTJ[78] and the extracted parameters are $E_F = 2.25$ eV, $U = 1$ eV, $d = 1$ nm, $m = 1.3m_e, m^* = 0.32m_e$ where m_e is the vacuum electron mass (See section 1.2 for the definition of other parameters). For an applied positive voltage, majority electrons from the fixed layer tunnel through the barrier and accumulate at the insulator-free layer interface, as shown in Fig 3b. After enough majority spin accumulates to overwhelm the minority spin density, the torque suffices to start switching the free layer from AP-to-P configuration at 2.6 ns. By 5 ns, the magnetization of the free layer has completed its switching from AP-to-P mode.

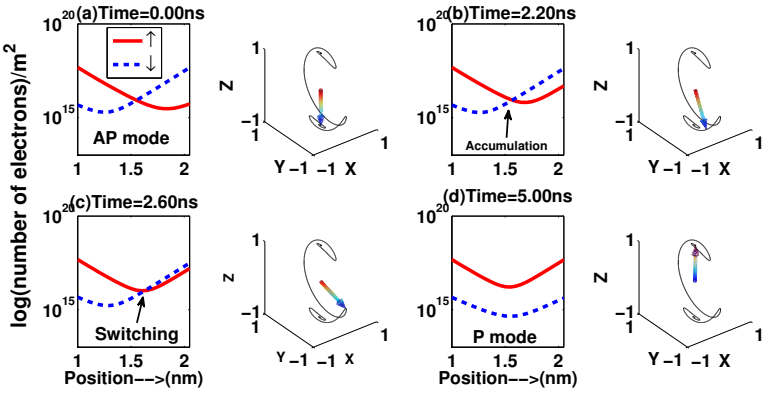

Figure 1.20 AP to P switching at 0.3V. The free layer and insulator interface is at position 2nm. (a)Time=0ns: The free-layer is anti-parallel to the fixed layer, (b) Time=2.2ns: Majority electrons with respect to the fixed layer tunnel through the barrier and accumulate at the insulator-fixed layer interface. The accumulated majority electrons exerts a torque on the free layer which causes its magnetization to switch. (c)Time=2.6ns: The free layer switching from anti-parallel to parallel configuration. (d)Time=5ns: The final magnetization of the free layer is parallel to the fixed layer.

Conversely for P-to-AP switching, a negative voltage is applied to the free layer, which is nearly parallel to the fixed layer. At 6ns, there is an accumulation of minority electrons at the insulator-fixed layer interface as the majority carriers get siphoned away. After enough minority spin accumulates to overwhelm the majority spin density, the torque starts switching the free layer from P-to-AP configuration at 7.6 ns. By 8 ns, the magnetization of the free layer has completed its switching from P-to-AP. Note that for the same bias magnitude, the anti-parallel to parallel switching occurs much faster than parallel to anti-parallel switching (conversely, the voltage required to switch within the same time pulse is larger for P-to-AP). We explained this asymmetry in section 1.2.1.3 as arising from energy asymmetry, since the addi-

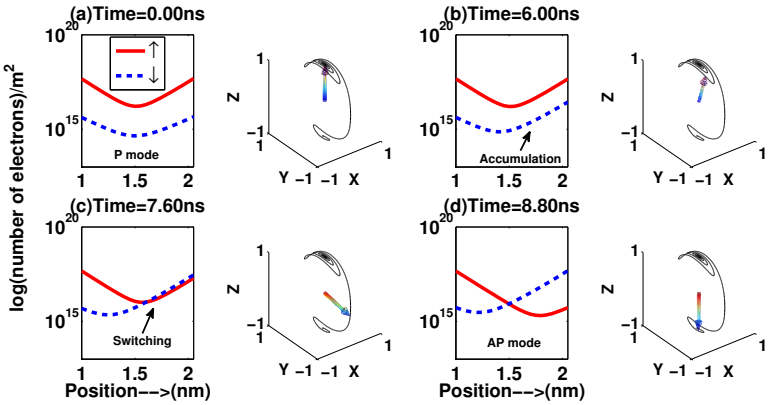

Figure 1.21 P to AP switching at -0.4V. The free layer and insulator interface is at position 2nm. (a)Time=0ns: The free-layer is parallel to the fixed layer, (b) Time=6ns: Minority electrons with respect to the free layer tunnel through the barrier, reflect back from the fixed layer and insulater interface, and accumulate at the insulator-fixed layer interface. The accumulated minority electrons exerts a torque on the free layer which causes its magnetization to switch. (c)Time=7.6ns: The free layer switching from parallel to anti-parallel configuration. (d)Time=8ns: The final magnetization of the free layer is anti-parallel to the fixed layer.

tion and removal of majority spins involve complementary energy states in the fixed layer, below vs above its Fermi energy with higher vs lower net electron polarization.

1.4.3 Including thermal fluctuations: stochastic LLG vs Fokker Planck

As mentioned earlier, thermal noise plays an important role in initiating the magnetization switching. This section will discuss how to incorporate thermal effects in the otherwise deterministic LLG equation 1.39, in order to analyze the dependence of error rate on thermal noise. The effect of thermal noise is two-fold. First, thermal noise creates a Boltzmann distribution of its initial angle that helps nudge the magnetization out of stagnation points where the contacts are precisely collinear. Thereafter, thermal noise compromises the evolution of the magnetization by introducing a net diffusive component in the microspin dynamics. To capture all these effects of thermal noise, a Langevin random field $\vec{H}_L$ is added to the effective magnetic field to represent the thermal perturbation,

$$\frac{d\vec{m}}{dt} = -\gamma\vec{m} \times \left(\vec{H}_{eff} + \vec{H}_L\right) + \alpha\left(\vec{m} \times \frac{d\vec{m}}{dt}\right) + \vec{\tau}_s \tag{1.42}$$

where

$$\vec{H}_L = \sqrt{\frac{2\alpha k_B T}{\mu_0 \gamma \Omega M_s}}\vec{G} \tag{1.43}$$

with k_B the Boltzman constant and $\vec{G}$ a three dimensional gaussian white noise with mean $\langle G(t) \rangle = 0$ and standard deviation of $\langle G^2(t) \rangle = 1$. One way to solve the stochastic LLG equation is to run it for a large number of $\vec{H}_L$ with a random number generator, and then take the time average. The error rate can be extracted easily from the distribution of magnetization orientation at given time. It is worth mentioning that the noise in stochastic LLG is multiplicative and a proper discretization scheme is necessary. Two common schemes (Ito and Stratonovich prescription) are used in literature. Here we solve the stochastic LLG in spherical coordinates within the Ito prescription[76] and validate our approach by comparing a separate evaluation of the Fokker-Planck equation, described below.

Instead of the stochastic evolution of the magnetization under individual thermal kicks, we can alternately track the evolution of the entire distribution function on the spherical surface, leading to the Fokker-Planck equation (FPE) [79]. Let us first recast the LLG equation in the form

$$\frac{\partial \vec{m}}{\partial t} = \mathcal{L}(\vec{m}) - \gamma \left[\vec{m} \times \vec{H}_L \right] \tag{1.44}$$

with $\mathcal{L}(\vec{m})$ being all the deterministic torques from LLG equation,

$$\mathcal{L}(\vec{m}) = \mathcal{L}_H(\vec{m}) + \vec{\tau}_S(\vec{m}) \tag{1.45}$$

where $\mathcal{L}_H(\vec{m})$ includes the torques $\hat{m} \times \vec{H}_{eff}$ from effective field, $\hat{m} \times (\hat{m} \times \vec{H}_{eff})$ from damping and $\vec{\tau}_s(\vec{m})$ from the spin transfer torque. The corresponding Fokker-Planck equation can then be derived from the Gaussian distributed multiplicative white noise as

$$\frac{\partial P}{\partial t} = -\vec{\nabla} \cdot (\mathcal{L}P) + D\nabla^2 P \tag{1.46}$$

where the effective 'diffusion coefficient' D is given by

$$D = \frac{\alpha \gamma k_B T}{(1+\alpha^2)\mu_0 M_s \Omega} \tag{1.47}$$

It is clear that we have switched variables from the magnetization $\vec{M}(t)$ in stochastic LLG to the distribution function of magnetization $P(\vec{M}, t)$ in FPE. Since the torques are perpendicular to $\hat{m}$, the saturation magnetization stays constant and $P(\vec{M}, t)$ becomes a function of the orientation $P(\theta, \phi, t)$ in spherical coordinates.

Eq 1.46 can be numerically solved by the finite element Galerkin technique [81] to give us the time evolution of $P(\theta, \phi, t)$ on a spherical surface. Fig 1.22 shows case studies for our 2D Fokker-Planck solver applied to a few simple systems. The write error rate (WER) can be calculated from the numerically extracted $P(\theta, \phi, t)$ by integrating the probability density over the hemisphere ($\theta < \pi/2$),

$$P_{WER}(t) = \int_0^{\pi/2} \int_0^{2\pi} P(\theta, \phi, t) \sin\theta d\phi d\theta \tag{1.48}$$

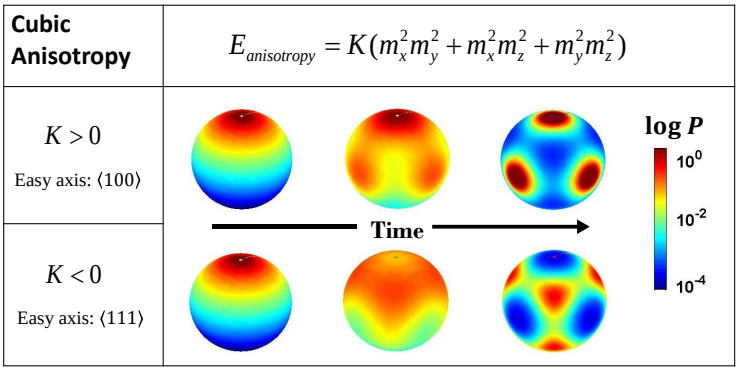

Figure 1.22 (color online) Probability distribution of magnetization in cubic anisotropic systems. Calculation starts with magnetization pointing at north pole (Gaussian distribution) and then relaxes to easy axis by the magnetic anisotropy field at long time limit.

The Fokker-Planck equation is expected to yield comparable error rates as a brute force solution of the stochastic LLG equation. However, it avoids having to solve the latter millions of times to develop a statistics over time. Moreover for systems with simple symmetry, it is amenable to analytical solutions. For instance, a perpendicular MTJ with uni-axial anisotropy has cylindrical symmetry and its solution is independent of the azimuthal angle $P(\theta, \phi, t) = P(\theta, t)$. The 2-D FPE then reduces to a 1-D equation and can be solved in an approximate analytical form for high overdrive currents to get a write error rate [80]:

$$WER(t) = 1 - exp\left[\frac{-\pi^2 \Delta(i-1)}{ie^{2\alpha\gamma H_k t(i-1)/(1+\alpha^2)} - 1}\right], \quad i = I/I_{c0} \qquad (1.49)$$

where I is the current, I_{c0} is the critical current, and $\Delta = \mu_0 H_k M_s \Omega / 2k_B T$ is the thermal stability factor of the free layer that determines its static error rate and overall endurance.

Fig 1.23 shows a comparison among a numerical multimillion trial solution of the stochastic LLG, a numerical solution of the FPE and the analytical approximation in Eq. 1.49 for a perpendicular magnet. The stochastic LLG and numerical FPE give the same result, while the analytical result overestimates the error for low switching currents. As expected, the switching time or the error rate can be reduced by increasing the scaled current overdrive $i = I/I_{c0}$, at the expense of an energy cost. The numerical FPE offers an efficient route to estimating this error rate towards a proper understanding of the delay-error-dissipation trade-offs and device to device fluctuations. An example of such analysis for perpendicular STT-MRAM cell based on analytical Fokker-Planck equation can be found in reference [16].

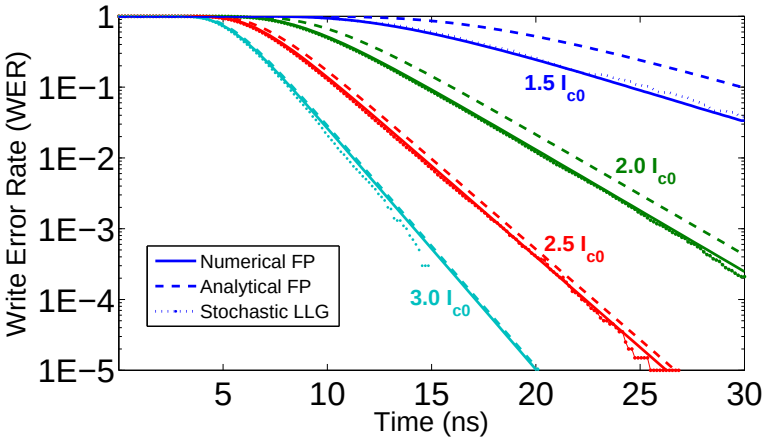

Figure 1.23 Write Error Rate for various switching current in a perpendicular MTJ. The perpendicular anisotropy energy is $KV = 45k_BT$ and I_{c0} is the intrinsic critical current calculated from LLG equation. Dotted line is for stochastic LLG, Solid line is for numerical Fokker-Planck and dashed line is for analytical approximation.

1.5 Summary: Multiscaling from atomic structure to error rate

Combining all the tools discussed so far, we can now build a predictive material-based approach for STT evaluation. The WERs for perpendicular materials has been observed to be quite low [82], bringing back attention to the write current and the need for a high TMR at room temperature. Both read and write currents depend on material properties that will need to be optimized going ahead[84]. A high throughput computational study of the combinatorial material phase space has immense value, given that material development is a rather slow, meticulous and ultimately arduous process. A proper understanding of the interface structure and the role of defects can be quite critical to progress. The atomic structure of the junction can be constructed either from experimental references or from the lowest energy optimized structure in DFT, along with evaluation of thermal stability and heats of formation. From the atomic structure, the electronic structure and system Hamiltonian are evaluated. The same Hamiltonian is then used to construct the Green's function of the MTJ, which contains all the necessary information for charge/spin current. The tunneling current and spin transfer torque can be evaluated thereafter with their full angular and voltage dependence and fed into the LLG solver which also takes into account other physical parameters such as the geometry of the magnet, external field and thermal noise. Solving the magnetization dynamics self consistently with the spin transfer torque ultimately provides useful information such as critical switching current, switching time and read/write error rates.

Figure 1.24 shows a demonstration of this integrated approach for an in-plane Fe/MgO (4 layers)/Fe tunnel junction. For Fe/MgO/Fe, the parameters are taken from [83] with a 170nm $\times$ 90nm $\times$ 3nm free layer, saturation magnetization $Ms = 1430$ emu/cm^3 and in-plane uni-axial anisotropy with stability factor $\Delta = K\Omega/k_BT = 30$. The figure shows the computed IV obtained first principles from our DFT STT + LLG simulation. The voltage is swept from -0.5 V to 0.5 V and then back to -0.5 V. A hysteresis shows up in the IV, signifying the switching of free layer. The AP-to-P and P-to-AP switching show up at around 200 mV and the critical current density is about 2.3×10^{11}A/m, close to the intrinsic critical current estimated from [83]. Notice that the ab-initio spin transfer torque is calculated from an ideal Fe/MgO/Fe junction with perfect interface so the I_p/I_{AP} is much higher than experimental value, the latter being very sensitive to interfacial defects and scattering. Such a scattering process affects the small minority spin current, so that the majority STT is still expected to be preserved in the presence of scattering.

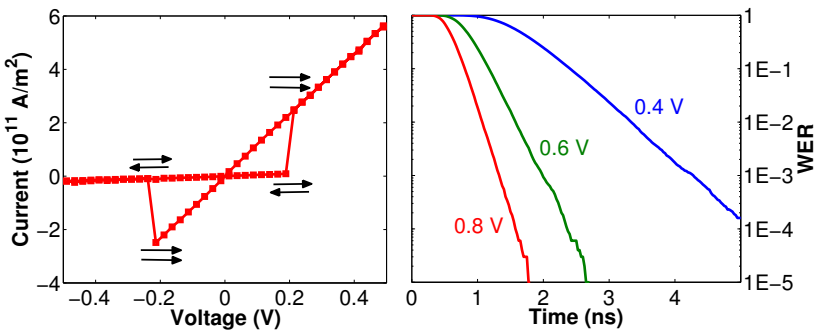

Figure 1.24 Ab-initio STT + Stochastic LLG simulation. Left: I-V characteristics for in-plane FeMgOFe MTJ. Black arrows indicate the relative configuration for the magnetization of the fixed/free layer. Right: error-delay plot at different voltage.

Figure 1.25 shows a further comparison of error rates between Fe/MgO(6 layer)/Fe and CoFe/MgO(6 layer)/FeCo in perpendicular MTJs (Experimental FeMgOFe MTJs usually have in-plane configuration because of high M_s. Here we assume a perpendicular FeMgOFe in order to compare with the state of art perpendicular CoFeMgOFeCo MTJ). In the simulation, the free layer is set to be a nano-cylinder with diameter 45 nm and thickness 2 nm. The perpendicular anisotropy is set to create an energy barrier with stability ratio $\Delta = 45$. The error rate is plotted as a function of switching time. The long lognormal tail arises from stagnation when the torque vanishes, requiring the current to be significantly higher than the critical current at a corresponding immodest dissipation cost. The ab-initio STT results indicate that CoFe has a higher in-plane torque than Fe (out-of-plane torque doesn't affect switching time in perpendicular systems). The big difference in error-delay plot is also due

to different saturation magnetizations M_s (1430 emu/cm^3 for Fe and 1050 emu/cm^3 for CoFe).

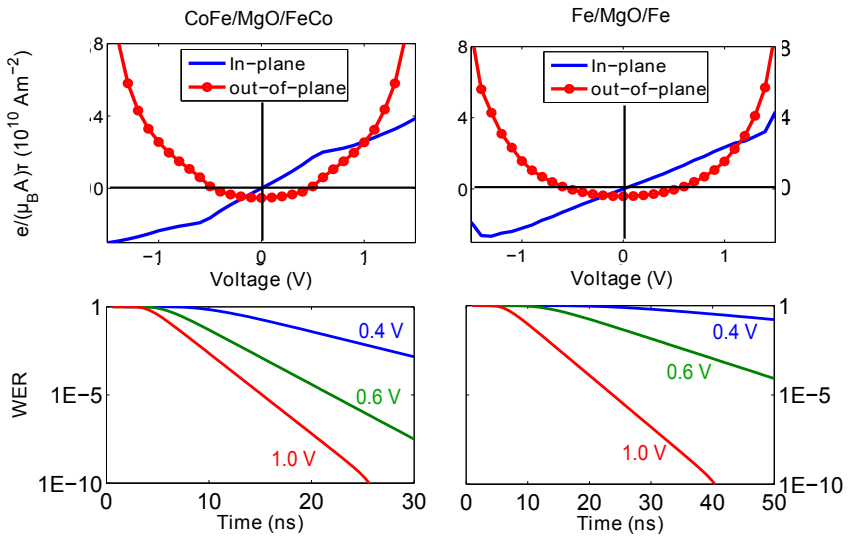

Figure 1.25 Ab-initio STT + Fokker-Planck simulation. Top-left: Ab-initio STT for CoFe/MgO/FeCo. Bottom-left: Error-delay for perpendicular CoFe/MgO/FeCo. Top-right: Ab-initio STT for Fe/MgO/Fe. Bottom-right: Error-delay for perpendicular Fe/MgO/Fe.

The figure is quite instructive. Given an acceptable write error and a delay (err and τ_0), we can use the curves to read off the switching current from the error-delay and the switching voltage from the corresponding IV plot. The energy dissipation is calculated using $E(err) = IV\tau_0$. If the material parameters are given, we can then use the analytical equation 1.40 and 1.49 to get the critical current and error rate, solve for the switching voltage by inverting the MTJ Simmons IV (eq 1.5 after integrating over transverse $k_{||}$ [20]). Fig.1.26 shows an example of such analysis based on analytical expressions[16]. The switching delay corresponding to the lowest energy dissipation can be identified for any given configuration and be extrapolated for nearby parameters (shown by the solid black line in Fig.1.26).

The purpose of this chapter is to illustrate the various aspects of an STT device, brought out by an integrated modeling platform that connects the atomic geometry with its electronic structure, quantum kinetics, stochastics and micromagnetics. At the level of atomic structure, we saw how the energy, orbital chemistry and spin texture of the contact and insulator bands promote a high spin filtering and a correspondingly large TMR (reducing the corresponding read current). The calculated

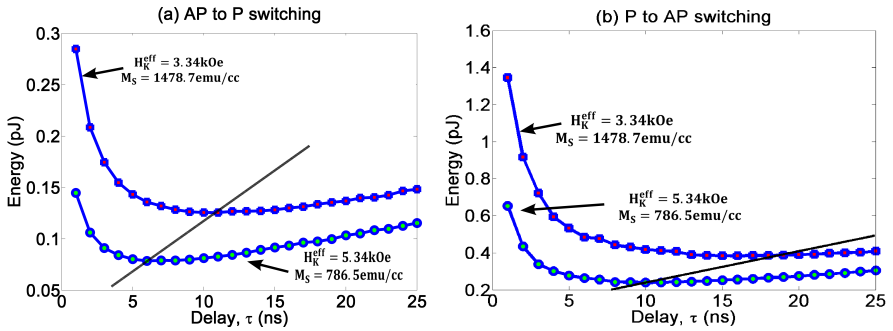

Figure 1.26 Energy-delay plot calculated from the analytical approximation for a perpendicular MTJ with different magnetic properties. Figure reprinted with permission from Electron Devices, IEEE Transactions on

TMR is however compromised by the interfacial structure, especially due to defects created by oxygen vacancies. The write operation is driven primarily by the current driven torque through the change in majority spin angular momentum at the free magnetic layer. The calculated torque enters the macrospin LLG solver to describe the destabilization, precession and ultimately the flipping of the spin beyond a certain threshold, with the error and speed dependent on the scaled current overdrive. The error arises because of stagnation points along the magnet's conformational potential landscape where we have a precise cancellation of the precessional torque, needing thermal kicks to dislodge the spins thereafter. Further exploration is needed how to fully understand the tradeoffs, such as how to reduce the critical current and switching voltage through material engineering, or the switching delay and error rate using approaches such as hybrid switching with a field assist to eliminate stagnation, or perhaps multidomain incoherent switching schemes.

1.6 Acknowledgements

We acknowledge generous support from the NSF NEB award under Grand Number 1124714 and the NSF DMREF award under Grand Number 1235230 for this project. I. Rungger acknowledges financial support from KAUST (ACRAB grant). M. Stamenova acknowledges financial support through the Eu-FP7 project CRONOS. Computational ressources have been provided by the Trinity Centre for High Performance Computing and the Irish Centre for High-End Computing. We acknowledge discussions with Prof. W. B Butler, C. Mewes, P. Visscher, E. Chen, S. Wolf, J. Lu, MA Stan, S. Bandyopadhyay and J. Atulasimha.

REFERENCES

1. Salahuddin, Sayeef, and Supriyo Datta.'Interacting systems for self-correcting low power switching' *Applied Physics Letters*, 90:093503, 2007.
2. Apalkov, Dmytro, et al. 'Spin-Transfer Torque Magnetic Random Access Memory (STT-MRAM)' *ACM Journal on Emerging Technologies in Computing Systems* 9:13, 2013.
3. Tehrani, Saied, et al. 'Magnetoresistive random access memory using magnetic tunnel junctions' *Proceedings of the IEEE* 91:703, 2003.
4. Kishi, T., et al. 'Lower-current and fast switching of a perpendicular TMR for high speed and high density spin-transfer-torque MRAM' *Electron Devices Meeting, IEDM* 2008.
5. Katine, J. A., et al. 'Current-Driven Magnetization Reversal and Spin-Wave Excitations in Co /Cu /Co Pillars' *Physical Review Letters* 84:3149, 2000.
6. Sun, J. Z., et al. 'Batch-fabricated spin-injection magnetic switches' *Applied Physics Letters* 81:2202, 2002.
7. Pantel, D., et al. 'Reversible electrical switching of spin polarization in multiferroic tunnel junctions' *Nature materials* 11:289, 2012.
8. Cherifi, R. O., et al.'Electric-field control of magnetic order above room temperature' *Nature materials* 13:345, 2014.
9. Liu, Luqiao, et al. 'Spin-Torque Switching with the Giant Spin Hall Effect of Tantalum' *Science* 336:555-558, 2012.

By author Copyright © 2014 John Wiley & Sons, Inc.

10. Slonczewski, John C. 'Initiation of spin-transfer torque by thermal transport from magnons' *Physical Review B* 82 (2010): 054403.

11. Fashami, M. S., Atulasimha, J., Bandyopadhyay, S. 'Magnetization dynamics, throughput and energy dissipation in a universal multiferroic nanomagnetic logic gate with fan-in and fan-out' *Nanotechnology*, 23:105201, 2012.

12. Kiselev, S. Il, et al. 'Microwave oscillations of a nanomagnet driven by a spin-polarized current' *Nature* 425: 380-383, 2003.

13. Shim, Seung-Bo, Matthias Imboden, and Pritiraj Mohanty.'Synchronized Oscillation in Coupled Nanomechanical Oscillators' *Science* 316: 95-99, 2007.

14. Behin-Aein, Behtash, et al. 'Proposal for an all-spin logic device with built-in memory' *Nature nanotechnology* 5: 266-270, 2010.

15. Ikeda, S., et al. "A perpendicular-anisotropy CoFeBMgO magnetic tunnel junction." *Nature materials* 9.9: 721-724, 2010.

16. Munira, Kamaram, William H. Butler, and Avik W. Ghosh. 'A Quasi-Analytical Model for Energy-Delay-Reliability Tradeoff Studies During Write Operations in a Perpendicular STT-RAM Cell' *Electron Devices, IEEE Transactions on* 59:2221, 2012.

17. Munira, Kamaram, Jonathon Romero, and William H. Butler.'Achieving perpendicular anisotropy in half-metallic Heusler alloys for spin device applications' *Journal of Applied Physics* 115: 17B731, 2014.

18. W. H. Butler, X.-G. Zhang, T. C. Schulthess, and J. M. MacLaren.'Spin-dependent tunneling conductance of Fe—MgO—Fe sandwiches' *Phys. Rev. B*, 63:054416, 2001.

19. Djayaprawira, David D., et al. '230% room-temperature magnetoresistance in CoFeB/MgO/CoFeB magnetic tunnel junctions' *Applied Physics Letters* 86:092502, 2005.

20. Slonczewski, John C. 'Conductance and exchange coupling of two ferromagnets separated by a tunneling barrier' *Physical Review B* 39:6995, 1989.

21. J. C. Slonczewski. 'Currents, torques, and polarization factors in magnetic tunnel junctions' *Phys. Rev. B*, 71: 024411, 2005.

22. Bruno, P. 'Interlayer exchange coupling: a unified physical picture' *Journal of magnetism and magnetic materials* 121:248, 1993.

23. Li, Z., et al. 'Perpendicular Spin Torques in Magnetic Tunnel Junctions' *Physical review letters* 100: 246602, 2008.

24. Datta, Deepanjan, et al. 'Voltage Asymmetry of Spin-Transfer Torques' *Nanotechnology, IEEE Transactions on* 11:261, 2012.

25. Theodonis, Ioannis, et al. 'Anomalous Bias Dependence of Spin Torque in Magnetic Tunnel Junctions' *Physical review letters* 97: 237205, 2006.

26. Tang, Y-H., et al. 'Influence of asymmetry on bias behavior of spin torque' *Physical Review B* 81: 054437, 2010.

27. S. Yuasa, T. Nagahama, A. Fukushima, Y. Suzuki, and K. Ando. 'Giant room-temperature magnetoresistance in single-crystal Fe/MgO/Fe magnetic tunnel junctions' *Nature Materials*, 3:868, 2004.

28. S. S. P. Parkin, C. Kaiser, A. Panchula, P. M. Rice, B. Hughes, M. Samant, and S.-H. Yang. 'Giant tunnelling magnetoresistance at room temperature with MgO (100) tunnel barriers' *Nature Materials*, 3:862, 2004.

29. S. Ikeda, J. Hayakawa, Y. Ashizawa, Y. M. Lee, K. Miura, H. Hasegawa, M. Tsunoda, F. Matsukura, and H. Ohno. 'Tunnel magnetoresistance of 604% at 300K by suppression of Ta diffusion in CoFeB/MgO/CoFeB pseudo-spin-valves annealed at high temperature' *Appl. Phys. Lett.*, 93:082508, 2008.

30. Y. M. Lee, J. Hayakawa, S. Ikeda, F. Matsukura, and H. Ohno.'Effect of electrode composition on the tunnel magnetoresistance of pseudo-spin-valve magnetic tunnel junction with a MgO tunnel barrier' *Appl. Phys. Lett.*, 90:212507, 2007.

31. S. Yuasa and D. D. Djayaprawira.'Giant tunnel magnetoresistance in magnetic tunnel junctions with a crystalline MgO(001) barrier' *J. Phys. D: Appl. Phys.*, 40:R337, 2007.

32. C. Tiusan, F. Greullet, M. Hehn, F. Montaigne, S. Andrieu, and A. Schuhl. 'Spin tunnelling phenomena in single-crystal magnetic tunnel junction systems' *J. Phys.: Condens. Matter*, 19:165201, 2007.

33. S. Datta. ' Electronic Transport in Mesoscopic Systems'. *Cambridge University Press, Cambridge*, UK, 1995.

34. A. R. Rocha, V. M. Garcia-Suarez, S. Bailey, C. Lambert, J. Ferrer, and S. Sanvito, 'Spin and molecular electronics in atomically generated orbital landscapes' *Phys. Rev. B*, 73: 085414 , 2002.

35. J. M. Soler, E. Artacho, J. D. Gale, A. Garcia, J. Junquera, P. Ordejon, and D. Sanchez-Portal, 'The SIESTA method for ab initio order-N materials simulation' *J. Phys.: Condens. Matter*, 14: 2745, 2002.

36. N.H. Mott, 'The electrical conductivity of transition metals' *Proc. Roy. Soc. A* **153**, 699 (1936)

37. J. Mathon and A. Umerski. 'Theory of tunneling magnetoresistance of an epitaxial Fe/MgO/Fe(001) junction' *Phys. Rev. B*, 63:220403(R), 2001.

38. K. D. Belashchenko, J. P. Velev, and E. Y. Tsymbal. 'Effect of interface states on spin-dependent tunneling in FeMgOFe tunnel junctions' *Phys. Rev. B*, 72:140404(R), 2005.

39. D. Wortmann, G. Bihlmayer, and S. Blügel. 'Ab initio calculations of interface effects in tunnelling through MgO barriers on Fe(100)' *J. Phys.: Condens. Matter*, 16:S5819, 2004.

40. C. Heiliger, P. Zahn, B. Y. Yavorsky, and I. Mertig. 'Influence of the interface structure on the bias dependence of tunneling magnetoresistance' *Phys. Rev. B*, 72:180406(R), 2005.

41. C. Heiliger, P. Zahn, B. Y. Yavorsky, and I. Mertig. 'Thickness dependence of the tunneling current in the coherent limit of transport' *Phys. Rev. B*, 77:224407, 2008.

42. W. H. Butler. 'Tunneling magnetoresistance from a symmetry filtering effect' *Sci. Technol. Adv. Mater.*, 9:014106, 2008.

43. P. K. de Boer and R. A. de Groot. 'The conduction bands of MgO, MgS and HfO2' *J. Phys.: Condens. Matter*, 10:10241, 1998.

44. Y. Fei. 'Effects of temperature and composition on the bulk modulus of (Mg,Fe)O' *Am. Mineral.*, 272:84, 1999.

45. D. M. Roessler and W. C. Walker. 'Electronic Spectrum and Ultraviolet Optical Properties of Crystalline MgO' *Phys. Rev.*, 159:733, 1967.

46. H. Baltache, R. Khenata, M. Sahnoun, M. Driz, B. Abbar, and B. Brouhafs. 'Full potential calculation of structural, electronic and elastic properties of alkaline earth oxides MgO, CaO and SrO' *Physica B*, 344:334, 2004.

47. J. Izquierdo, A. Vega, L. C. Balbas, D. Sanchez-Portal, J. Junquera, 'Systematic ab initio study of the electronic and magnetic properties of different pure and mixed iron systems' E. Artacho, J. M. Soler, and P. Ordejon. *Phys. Rev. B*, 61:13639, 2000.

48. Webelements: the periodic table on the web.

49. A. M. Turner, A. W. Donoho, and J. L. Erskine. 'Experimental bulk electronic properties of ferromagnetic iron' *Phys. Rev. B*, 29:2986, 1984.

50. J.-H. Cho and M. Scheffler. 'Ab initio pseudopotential study of Fe, Co, and Ni employing the spin-polarized LAPW approach' *Phys. Rev. B*, 53:10685, 1996.

51. J. Callaway and C. S. Wang. Energy bands in ferromagnetic iron. 'Energy bands in ferromagnetic iron' *Phys. Rev. B*, 16(5):2095–2105, Sep 1977.

52. S. Sanvito. In Handbook of Computational Nanotechnology. American Scientific, Stevenson Ranch, CA, 2005. Vol. 5; Also available at cond-mat/0503445.

53. A.R. Rocha, V.M. Garcia-Suarez, S.W. Bailey, C.J. Lambert, J. Ferrer, and S. Sanvito. 'Towards molecular spintronics' *Nature Materials*, 4:335, 2005.

54. P. J. Zermatten, G. Gaudin, G. Maris, M. Miron, A. Schuhl, C. Tiusan, and M. Greullet, F. Hehn. 'Experimental evidence of interface resonance states in single-crystal magnetic tunnel junctions' *Phys. Rev. B*, 78:033301, 2008.

55. I. Rungger, O. Mryasov, and S. Sanvito, 'Resonant electronic states and I-V curves of Fe/MgO/Fe(100) tunnel junctions' *Phys. Rev. B*, 79:094414, 2009.

56. X.-G. Zhang, W. H. Butler, and Amrit Bandyopadhyay. 'Effects of the iron-oxide layer in Fe-FeO-MgO-Fe tunneling junctions' *Phys. Rev. B*, 68:092402, 2003.

57. P. Bose, A. Ernst, I. Mertig, and J. Henk. 'Large reduction of the magnetoresistance in Fe/MgO/Fe tunnel junctions due to small oxygen concentrations at a single FeO interface layer: A first-principles study' *Phys. Rev. B*, 78:092403, 2008.

58. V. M. Xu, P. X. andKarpan, K. Xia, M. Zwierzycki, I. Marushchenko, , and P. J. Kelly. 'Influence of roughness and disorder on tunneling magnetoresistance' *Phys. Rev. B*, 73:180402(R), 2006.

59. M. Müller, F. Matthes, and C. M. Schneider. 'Spin polarization at ferromagnet-insulator interfaces: The important role of stoichiometry in MgO/Fe(001)' *Europhysics Lett.*, 80:17007, 2007.

60. P. G. Mather, J. C. Read, and R. A. Buhrman. 'Disorder, defects, and band gaps in ultrathin (001) MgO tunnel barrier layers' *Phys. Rev. B*, 73:205412, 2006.

61. M. Sterrer, M. Heyde, M. Novicki, N. Nilius, T. Risse, H.-P. Rust, G. Pacchioni, and H.-J. Freund. 'Identification of Color Centers on MgO(001) Thin Films with Scanning Tunneling Microscopy' *J. Phys. Chem. B (Letter)*, 110:46, 2006.

62. A. Gibson, R. Haydock, and J. P. LaFemina. 'Stability of vacancy defects in MgO: The role of charge neutrality' *Phys. Rev. B*, 50:2582, 1994.

63. B. M. Klein, W. E. Pickett, L. L. Boyer, and R. Zeller. 'Theory of F centers in the alkaline-earth oxides MgO and CaO' *Phys. Rev. B*, 35:5802, 1987.

64. G. Pacchioni. 'Modeling doped and defective oxides in catalysis with density functional theory methods: Room for improvements' *J. Chem. Phys.*, 128:182505, 2008.

65. J. P. Velev, K. D. Belashchenko, S. S. Jaswal, and E. Y. Tsymbal. 'Effect of oxygen vacancies on spin-dependent tunneling in Fe/MgO/Fe magnetic tunnel junctions' *Appl. Phys. Lett.*, 90:072502, 2007.

66. J. Ozeki, H. Itoh, and J. Inoue. 'Interfacial electronic structure and oxygen vacancy states in Fe/MgO/Fe tunneling junctions' *J. Magn. Magn. Mater.*, 310:e644, 2007.

67. G. X. Miao, Y. J. Park, J. S. Moodera, M. Seibt, G. Eilers, and M. Münzenberg. 'Disturbance of Tunneling Coherence by Oxygen Vacancy in Epitaxial Fe/MgO/Fe Magnetic Tunnel Junctions' *Phys. Rev. Lett.*, 100:246803, 2008.

68. T. N. Todorov. 'Tight-binding simulation of current-carrying nanostructures' *J. Phys.: Condens. Matter*, 14:3049, 2002.

69. R. Zhang, I. Rungger, S. Sanvito, and S. Hou. 'Current-induced energy barrier suppression for electromigration from first principles' *Phys. Rev. B*, 84: 085445, 2011.

70. I. Theodonis, N. Kioussis, A. Kalitsov, M. CHshiev, and W. H. Butler. 'Anomalous Bias Dependence of Spin Torque in Magnetic Tunnel Junctions' *Phys. Rev. Lett.*, 97: 237205, 2006.

71. A. Kalitsov, W. Silvestre, M. CHshiev, and J. P. Velev. 'Spin torque in magnetic tunnel junctions with asymmetric barriers' *Phys. Rev. B*, 88: 104430, 2013.

72. Heiliger, Christian, and M. D. Stiles. 'Ab initio studies of the spin-transfer torque in magnetic tunnel junctions.' *Physical review letters* 100.18: 186805, 2008

73. Jia, Xingtao, et al. 'Nonlinear bias dependence of spin-transfer torque from atomic first principles.' *Physical Review B* 84.1: 014401, 2011

74. Franz, Christian, Michael Czerner, and Christian Heiliger. 'Influence of the magnetic material on tunneling magnetoresistance and spin-transfer torque in tunnel junctions: Ab initio studies.' *Physical Review B* 88.9: 094421, 2013

75. C. Sankey, Y.-T. Cui, J. Z. Sun, J. C. Slonczewski, R. A. Buhrman, and D. C. Ralph. 'Measurement of the spin-transfer-torque vector in magnetic tunnel junctions' *Nature: Phys.*, 4: 67, 2008.

76. Aron, Camille, et al. 'Magnetization dynamics: path-integral formalism for the stochastic Landau-Lifshitz-Gilbert equation' *arXiv preprint* arXiv:1402.1200, 2014.

77. Sun, J. Z. 'Spin-current interaction with a monodomain magnetic body: A model study' *Physical Review B* 62:570, 2000.

78. Kubota, Hitoshi, et al. 'Quantitative measurement of voltage dependence of spin-transfer torque in MgO-based magnetic tunnel junctions' *Nature Physics* 4: 37, 2007.

79. Brown Jr, William Fuller. 'Thermal Fluctuations of a SingleDomain Particle' *Journal of Applied Physics* 34:1319, 2004.

80. Butler, W. H., et al. 'Switching Distributions for Perpendicular Spin-Torque Devices Within the Macrospin Approximation' *Magnetics, IEEE Transactions on* 48:4684, 2012.

81. K. Zhang, 'Thermal switching of a Stoner-Wohlfarth particle: Numerical solution of Fokker-Planck equation without symmetry' Ph.D. thesis, University of California, San Diego, 1998.

82. Nowak, J. J., et al. ”Demonstration of ultralow bit error rates for spin-torque magnetic random-access memory with perpendicular magnetic anisotropy.” *Magnetics Letters, IEEE* 2 (2011): 3000204-3000204.

83. Matsumoto, Rie, et al. ’Spin-torque-induced switching and precession in fully epitaxial Fe/MgO/Fe magnetic tunnel junctions’ *Physical Review B* 80:174405, 2009.

84. Munira, Kamaram, William A. Soffa, and Avik W. Ghosh. ’Comparative material issues for fast reliable switching in STT-RAMs’ *Nanotechnology, 2011 11th IEEE Conference on. IEEE,* 2011.